Structural Modeling of O/F Correlated Disorder in TaOF 3 and NbOF 3− x (OH) x by Coupling Solid-State NMR and DFT Calculations

Ouail Zakary, Monique Body, Thibault Charpentier, Vincent Sarou-Kanian, Christophe Legein

To cite this version:

Ouail Zakary, Monique Body, Thibault Charpentier, Vincent Sarou-Kanian, Christophe Legein. Structural Modeling of O/F Correlated Disorder in TaOF 3 and NbOF 3− x (OH) x by Coupling Solid-State NMR and DFT Calculations. Inorganic Chemistry, 2023, 62 (40), pp.16627-16640. ⟨10.1021/acs.inorgchem.3c02844⟩. ⟨hal-04250645⟩

HAL Id: hal-04250645
https://hal.science/hal-04250645v1

Submitted on 19 Oct 2023

Structural modeling of O/F correlated disorder in $TaOF_3$ and $NbOF_{3-x}(OH)_x$ by coupling solid state NMR and DFT calculations

Ouail Zakary[a,*], *Monique Body*[a,*], *Thibault Charpentier*[b], *Vincent Sarou-Kanian*[c], *Christophe Legein*[a]

[a] Institut de Molécules et Matériaux du Mans (IMMM) - UMR 6283 CNRS, Le Mans Université, Avenue Olivier Messiaen, 72805 Le Mans Cedex 9, France

[b] Université Paris-Saclay, CEA, CNRS, NIMBE, 91191, Gif-sur-Yvette cedex, France

[c] CNRS, CEMHTI UPR3079, Université d'Orléans, 45071 Orléans, France

KEYWORDS: heteroanionic compounds, correlated disorder, ^{19}F and ^{1}H solid-state NMR, DFT calculations, structural modeling

ABSTRACT. The structure of MOF_3 (M = Nb, Ta) compounds was precisely modeled by combining powder X-ray diffraction, solid-state NMR spectroscopy and semi-empirical dispersion corrected DFT calculations. It consists of stacked $_\infty(MOF_3)$ layers along the $\vec{c}$ direction formed by heteroleptic corner-connected MX_6 (X = O, F) octahedra. ^{19}F NMR resonance assignments and occupancy rates of the anionic crystallographic sites have been revised. The bridging site is shared equally by the anions and the terminal site is occupied by F only. An O/F correlated disorder is expected since *cis*-MO_2F_4 octahedra are favored, resulting in one-dimensional –F–M–O–M– strings along the <100> and <010> directions. Ten different 2×2×1 supercells per compound, fulfilling these characteristics, were built. Using DFT calculations and the GIPAW approach, the supercells were relaxed and the ^{19}F isotropic chemical shift values were determined. The agreement between the experimental and calculated ^{19}F spectra is excellent for $TaOF_3$. The ^{1}H and ^{19}F experimental NMR spectra revealed that some of the bridging F atoms are substituted by OH groups, especially in $NbOF_3$. New supercells involving OH groups were generated. Remarkably, the best agreement is obtained for the supercells with the composition closest to that estimated from the ^{19}F NMR spectra, *i.e.*, $NbOF_{2.85}(OH)_{0.15}$.

1. Introduction

Heteroanionic materials, such as oxyhalides, offer opportunities for developing new materials with targeted functionalities.[1] Understanding their properties requires a complete structural characterization. When these materials contain anions with similar X-ray or neutron scattering factors, such as oxides and fluorides, diffraction data alone is often insufficient to fully predict the anionic substructure. In these cases, if the anions are well-ordered, a complete structural model may be proposed by combining long-range diffraction data with bond-valence sum analysis. However, for those in which the different anions have joint occupancy of equivalent crystallographic sites, the structure cannot be fully described using a single unit cell, even if it does not necessarily imply a random distribution of the anions. Indeed, between the limits of fully ordered and randomly disordered anions, there are many cases of intermediate anion orders with local clustering or extended correlations that may give rise to non-random site occupancies in the averaged crystal structure.[1,2]

Pentavalent (Nb,Ta)-based inorganic oxyfluorides represent a rich family of compounds,[3] synthesized and structurally characterized from the 1950s to the 2000s, including NbO_2F,[4–7] TaO_2F,[4,8] Nb_3O_7F,[5,9,10] Ta_3O_7F,[8,11] $Nb_5O_{12}F$,[9] $Nb_{17}O_{42}F$ and $Nb_{31}O_{77}F$,[12,13] $Nb_3O_5F_5$,[14] and $NbOF_3$ and $TaOF_3$.[15] They exhibit interesting physical properties such as photocatalytic activity (MO_2F (M = Nb,[16,17] Ta[18,19]) and M_3O_7F (M = Ta,[19] Nb[17,20,21])), electrochromism (NbO_2F),[22] almost zero thermal expansion (TaO_2F),[23–25] and Li^+ intercalation (NbO_2F,[7,26,27] Nb_3O_7F[27,28]). Except in $Nb_{17}O_{42}F$[13] and MOF_3 (M = Nb, Ta)[15] crystal structures, O^{2-} and F^- are randomly distributed on all anion sites.[4,6,7,9–11,13,14] In $Nb_{17}O_{42}F$, O^{2-} and F^- are randomly distributed on only two of the anion sites, and in MOF_3, O^{2-} and F^- are preferentially distributed.

In disordered oxyfluorides, the short-range structures must deviate from the average crystal structures to accommodate the different M−O and M−F bond lengths. This has been indeed shown for MO_2F (M = Nb, Ta) and $Nb_3O_5F_5$ in four studies using various techniques: electron diffraction study of NbO_2F[29] and $Nb_3O_5F_5$[30] and variable-temperature neutron diffraction[23] and total X-ray scattering[25] studies of TaO_2F.

NbO_2F and TaO_2F both adopt an average cubic ReO_3-type structure. Brink et al.[29] have shown the coexistence in NbO_2F of (i) uncorrelated with each other one-dimensional O/F-ordered strings of atoms, −Nb−O−Nb−O−Nb−F−, with significant displacements of Nb from the ideal cation site, along the three ⟨001⟩ directions, and (ii) correlated rigid unit model (RUM) rotation of NbX_6 octahedra. It was suggested that the high transverse anisotropic displacement parameters, evidenced in TaO_2F, likely result from the static tilting of the TaO_4F_2 octahedra and Ta−(O/F)−Ta angles inferior to 180°.[23] In addition, Morelock *et al.*[25] demonstrated that a cubic 3×3×3 supercell model featuring −Ta−O−Ta−O−Ta−F− chains along the three ⟨001⟩ directions, with different Ta−O and Ta−F distances and O/F off-axis displacements, gave much better agreement with PDFs. Finally, the structural modeling of NbO_2F and TaO_2F by DFT geometry optimized supercells, supported by the very good agreement between experimental and calculated ^{19}F δ_{iso} values, leads to realistic disordered structures.[31]

$Nb_3O_5F_5$[14] is the n = 3 member of an $Nb_nO_{2n-1}F_{n+2}$ ($1 \leq n \leq \infty$) homologous series of oxyfluoride compounds. Their average structure consists of two-dimensional slabs regularly stacked along the *c* direction and shifted one from another by (1/2 *a* + 1/2 *b*). The thickness of each slab is formed by n octahedral layers of corner-linked $Nb(O,F)_6$ octahedra. The continuous planes of diffuse intensity observed by electron diffraction imply the existence of strings of ordered oxygen and fluorine atoms for equatorial anion sites along [100] and [010] albeit without correlation from one such string to the next, and octahedral rotation RUM modes of distortion, analogous to those observed in NbO_2F.[30] Additionally, a bond valence sum (BVS) argument has been used to derive a plausible site occupation model for the remaining apical and median anion sites.

MOF_3 (M = Nb, Ta), the n = 1 members of the $M_nO_{2n-1}F_{n+2}$ series, then adopt the SnF_4 type structure (tetragonal system, SG: *I*4/*mmm* (139)). The slabs consist of one octahedral layer formed by $MX1_{4/2}X2_2$ corner-linked octahedra, and are stacked, via van der Waals (vdW) interactions, along the $\vec{c}$ direction. According to Rietveld refinements of the powder X-Ray diffraction (PXRD) data, O and F atoms are distributed on both the bridging (X1) and the terminal (X2) sites with site occupancies significantly different for the two compounds : 0.725 F/0.275 O for X1 and 0.775 F/0.225 O for X2 in $NbOF_3$ and 0.90 F/0.10 O for X1 and 0.60 F/0.40 O for X2 in $TaOF_3$.[15] Furthermore, based on BVS calculations,[32,33] the authors conclude that F atoms should preferentially occupy the X2 site for both compounds. In contrast, their analysis of the ^{19}F NMR spectrum of $TaOF_3$ led them to conclude that the X2 site is preferentially occupied by O atoms. On the other hand, and in agreement with previous BVS calculations, Brink *et al.* predict that, in $NbOF_3$, the apical (terminal) X2 anion site is overwhelmingly occupied by F rather than O (0.523 F/0.477 O for X1 and 0.977 F/0.023 O for X2) along with a RUM rotation angle equal to 7.8°.[30]

To capture structural features of complex materials on various length scales and generate realistic models, the combination of complementary quantitative experimental measurements is crucial.[34] Both intermediate-range chemical disorder and short-range geometrical disorder give rise in local spectroscopies such as NMR to distributions of resonance frequencies. The prediction of the spectroscopic responses by means of electronic structure calculations therefore plays an essential role not only to assign the different spectral contributions, but also to understand the structural origins of the experimental parameter distributions.[35–39] This has been successfully exploited in numerous studies of disordered inorganic crystalline materials by coupling solid-state NMR and DFT calculations on supercells.[31,40–62]

Herein, we describe the structural modeling of $NbOF_3$ and $TaOF_3$. Based on BVS calculations,[33] and on experimental δ_{iso} and relative intensity values extracted from the ^{19}F NMR spectra, assignment of the resonances and occupancy rates of the two anion crystallographic sites have been revised.

The average structures issued from PXRD refinements were used to construct 2×2×1 supercells fulfilling the expected O/F correlated disorder. Three arrangements of O and F in the $(\vec{a},\vec{b})$ planes are possible and combining them results in ten possible models for each compound. All models were geometry optimized and magnetic shielding values were calculated using the GIPAW[63,64] approach, converted to chemical shifts and then compared to the experimental data. Despite the MOF_3 compounds being prepared using solid-state synthesis, the ^{1}H and ^{19}F experimental NMR spectra revealed that some of the bridging F1 atoms are substituted by OH groups, leading to the general formulation $MOF_{1-x}(OH)_xF_2$. Due to the higher OH group content in $NbOF_3$, a satisfactory agreement between experimental and calculated ^{19}F spectra could not be obtained without introducing OH groups in the models. Then, new models were built considering different OH substitution rates, and their influence on the calculated ^{1}H and ^{19}F spectra is evidenced.

2. Experimental details

2.1 Synthesis. $NbOF_3$ has been known since the second half of the 19th century.[65] A hundred years later its presence as a by-product was mentioned in two studies on NbO_2F[66] and NbF_3,[67] and then in the gas state as a product of the decomposition of NbO_2F.[5] MOF_3 (M = Nb, Ta) have been previously synthesized by Nieder-Vahrenholz *et al.*,[68] by reaction of MF_5 with oxide glass or M_2O_5 and by Köhler *et al.*[15] by reaction of MF_5 with MO_2F. The aqueous solution synthesis proposed by Frevel and Rinn,[4] which was used by Köhler *et al.* leads to compounds that both contain hydroxyl defects and metal vacancies.[31,68] Consequently, in the present work, MO_2F were prepared by solid-state synthesis from a mixture of MF_5 (Alfa Aesar, 99.9% and 99% for TaF_5 and NbF_5, respectively) and M_2O_5 (Alfa Aesar, 99.85% and 99.9% for Ta_2O_5 and Nb_2O_5, respectively) with an excess of MF_5 (5% and 10% for NbF_5 and TaF_5, respectively) relative to the ideal 2:1 molar ratio. M_2O_5 compounds were dried under secondary vacuum at 150 °C for 9 h with heating and cooling rates of 2 $°C.min^{-1}$, and then kept under nitrogen atmosphere inside a glove box before use. Considering the moisture sensitivity of MF_5, the steps of weighing, mixing and grinding were carried under nitrogen atmosphere using a glove box. The mixtures were then put inside platinum tubes, sealed and heated up to 210 °C for 18 h with a heating rate of 5 $°C.min^{-1}$ and then quenched in water at room temperature. MOF_3 were prepared from a mixture of MF_5 and MO_2F. The steps of weighing, mixing and grinding were carried under nitrogen atmosphere inside a glove box. The mixtures were then loaded in platinum tubes, sealed and heated at 210°C for 18 h with heating and cooling rates of 5 $°C.min^{-1}$. An excess of 10% of MF_5 relative to the molar 1:1 ratio is required to avoid the presence of unreacted MO_2F. The final products are sensitive to moisture.

2.2 Characterization techniques.

2.2.1 Powder X-ray diffraction. The PXRD patterns were recorded at room temperature with a PANalytical EMPYREAN diffractometer equipped with a PIXcel1D X-ray detector using monochromatic Cu K_α radiation ($\lambda = 1.5406$ Å). The samples were loaded in a domed sample holder using a glove box under nitrogen atmosphere. The patterns were measured in a 2θ range of 5° to ~120° with a 0.0131° step size. The recording time was approximately 6 h.

2.2.2 Solid-state NMR spectroscopy. Magic Angle Spinning (MAS) NMR spectra of ^{19}F and ^{1}H ($I = \frac{1}{2}$) were recorded with a Bruker Avance III spectrometer functioning at 4.7 T (^{19}F and ^{1}H Larmor frequencies of 188.3 MHz and 200 MHz, respectively) using a 1.3 mm CP-MAS probehead. The Hahn echo sequence was used with an interpulse delay of one rotor period and a recycle delay of 10 s and 5 s for ^{19}F and ^{1}H, respectively. For both nuclei, the 90° pulse was set to 1.5 µs, corresponding to a 167 kHz RF field. ^{19}F and ^{1}H spectra are referenced to $CFCl_3$ and tetramethylsilane, respectively. The ^{19}F chemical shift anisotropies were determined from the spinning sideband intensities according to Herzfeld and Berger.[70] ^{19}F "infinite spinning frequency" MAS spectra were obtained from the full projection (onto the frequency dimension) of a Two-dimensional One Pulse (TOP) spectrum issued from the stacking of subspectra shifted by the spinning frequency from the conventional MAS spectrum.[71] These "infinite spinning frequency" isotropic spectra allow a direct quantification of the inequivalent fluorine sites (environments) in the structure and represent an alternative to the simulation of the spinning sideband manifolds. The reconstructions of the one-dimensional MAS (including spinning sidebands) and the TOP processing spectra were performed with the DMFit software.[72]

3. Ab initio calculations

3.1 Definitions. The calculated magnetic shielding parameters are defined by the Haeberlen convention.[73] The isotropic magnetic shielding (σ_{iso}), the anisotropy of the magnetic shielding (σ_{CSA}) and the asymmetry parameter (η_{CSA}), are respectively defined as $\sigma_{iso} = (\sigma_{xx} + \sigma_{yy} + \sigma_{zz})/3$, $\sigma_{CSA} = \sigma_{zz} - \sigma_{iso}$ and $\eta_{CSA} = (\sigma_{yy} - \sigma_{xx})/\sigma_{CSA}$, with the magnetic shielding tensor components σ_{ii} defined in the sequence $|\sigma_{zz} - \sigma_{iso}| \geq |\sigma_{xx} - \sigma_{iso}| \geq |\sigma_{yy} - \sigma_{iso}|$. The chemical shift tensor is also defined by three parameters, the isotropic chemical shift (δ_{iso}), the anisotropy of the chemical shift (δ_{CSA}) and the asymmetry parameter (η_{CSA}), which are given by $\delta_{iso} = (\delta_{xx} + \delta_{yy} + \delta_{zz})/3$, $\delta_{CSA} = \delta_{zz} - \delta_{iso}$ and $\eta_{CSA} = (\delta_{yy} - \delta_{xx})/\delta_{CSA}$, with the chemical shift tensor components defined in the sequence $|\delta_{zz} - \delta_{iso}| \geq |\delta_{xx} - \delta_{iso}| \geq |\delta_{yy} - \delta_{iso}|$. The relation between the isotropic magnetic shielding and the isotropic chemical shift is $\delta_{iso} \approx \sigma_{ref} - \sigma_{iso}$.

3.2 DFT calculations. Solid-state DFT calculations with periodic boundary conditions were performed on 2×2×1 supercells (from 40 to 42 atoms). The ground state electronic structure was obtained by the generalized gradient approximation (GGA) using the Perdew-Burke-Ernzerhof (PBE) functional (GGA-PBE).[74] The atomic position optimization (APO) and the full optimization of the supercells (FO, relaxation of atomic positions and supercell parameters) were performed using the VASP package (6.2.1 version).[75,76] The projector augmented wave (PAW)[77,78] potentials used for Ta, Nb, F, O and H are respectively: Ta_sv_GW ($5s^2$ $5p^6$ $6s^2$ $5d^3$), Nb_sv_GW ($4s^2$ $4p^6$ $5s^1$ $4d^4$), F_GW ($2s^2$ $2p^5$), O_s_GW ($2s^2$ $2p^6$) and H_GW ($1s^1$). The wave functions were expanded on a plane-wave basis set with a 550 eV kinetic energy cut-off and (3×3×3) shifted Monkhorst-Pack k-point mesh. The total energy was converged up to change below 10^{-8} eV. Terminal F from different $_{\infty}(MOF_3)$ layers are weakly bonded to each other via vdW interactions. Since this interaction is not included in the standard DFT-GGA algorithm, zero damping semi-empirical dispersion correction of Grimme *et al.*[79] called DFT-D3 was included to the calculations. The damping function parameters (α_6, α_8, s_6, s_8, $s_{R,6}$ and $s_{R,8}$) were kept at the default values as well as the cut-off radius for pair interactions and the cut-off coordination radius. For both compounds, two methods of relaxation were performed, APO and FO, respectively referred in the following as APO_DFT-D3 and FO_DFT-D3.

The GIPAW approach[63,64] was used to calculate the magnetic shielding for the different nuclei, using the VASP package.[75,76] The PAW potentials, plane-wave energy cut-off and shifted Monkhorst-Pack k-point mesh were set to the same values as for the geometry optimization. NMR parameter calculations were performed on APO_DFT-D3 and FO_DFT-D3 supercells.

For ^{19}F in inorganic fluorides, several linear relationships between calculated σ_{iso} values, using the GIPAW approach, and experimental δ_{iso} values, $\delta_{iso} = \sigma_{ref} - a\ \sigma_{iso}$, have been established to convert calculated σ_{iso} values into "calculated" δ_{iso} values. The absolute values of the slopes depend on the metal atom(s) constituting the fluoride(s) and are often significantly less than 1.[80–92] Then, in this paper, distinct $\delta_{iso} = \sigma_{ref} - a\ \sigma_{iso}$, equations determined by linearly correlating the calculated σ_{iso} values to the experimental δ_{iso} values[83] of NbF_5 and TaF_5, are used for $NbOF_3$ and $TaOF_3$, respectively, as previously done for NbO_2F and TaO_2F.[31] Since the previous $\delta_{iso} = \sigma_{ref} - a\ \sigma_{iso}$ equations[83] have been established using the CASTEP code,[93,94] to ensure the consistency of our calculations, new linear regressions were determined using the VASP package and keeping the conditions used for calculations on MOF_3 supercells. These linear regressions are discussed in further detail later on in the paper (see **4.5**). The ^{1}H δ_{iso} calculated values were deduced using the equation: δ_{iso} (ppm) $= -\ \sigma_{iso} + 31$.[95]

4. Results and discussion

4.1 Structural characterization: solid state NMR.

For (oxy)fluorides, ^{19}F solid-state NMR is the ideal technique for determining the proportion of fluorine atoms in each crystallographic site (in each different environment) through the relative intensities of the NMR lines. The ^{19}F MAS NMR spectra of $NbOF_3$ and $TaOF_3$ are presented in **Figure 1**. Their fits, those of the corresponding ^{19}F "infinite spinning frequency" isotropic spectra and the corresponding fit parameters are reported in SI (**Figures S1-S4** and **Tables S1-S4**). The parameters relevant for the discussion are gathered in **Table 1**. Both ^{19}F MAS NMR spectra present two main resonances, one more intense with higher δ_{iso} and δ_{CSA} values and one less intense with lower δ_{iso} and δ_{CSA} values, as well as additional low intensity resonances located in between but closer to the more intense. For both compounds the less intense ^{19}F main resonance is assigned to the X1 (bridging) anion site and the more intense ^{19}F main resonance, as well as the additional low intensity resonances, are assigned to the X2 (terminal) anion site (**Table 1**). These assignments are the opposite of those published previously.[15] However they are supported by the evolution of the ^{19}F δ_{iso} values with the number of surrounding cations. For a given cation, the higher the coordination number, the lower the ^{19}F δ_{iso} values,[31,96] as observed, for instance, in NbF_5 (bridging: -42 ppm; terminal: 193 to 268 ppm), TaF_5 (bridging: -70 ppm; terminal: 106 to 174 ppm).[83] and TiF_4 (bridging: -2 to 30 ppm; terminal: 422 to 479 ppm).[90] These assignment are also supported by the higher δ_{CSA} values of the resonances assigned to the terminal F atoms, as also observed for instance in NbF_5, TaF_5[83] and TiF_4,[90] the environment of a terminal F atom being more anisotropic than the environment of a bridging F atom surrounded by two identical cations located approximately opposite each other.

If we assume that the X2 site is fully occupied by F, and thus that the X1 site is half occupied by F and O atoms, the relative intensities of the corresponding NMR lines should be 2/3 for the terminal F2 NMR line and 1/3 for the bridging F1 one. $NbOF_3$ and $TaOF_3$ being moisture sensitive, the most likely hypothesis to explain that the relative intensities of the bridging F1 NMR lines are less than 1/3 (**Table 1**) is the substitution of a part of the F atoms of the bridging X1 site by OH groups.

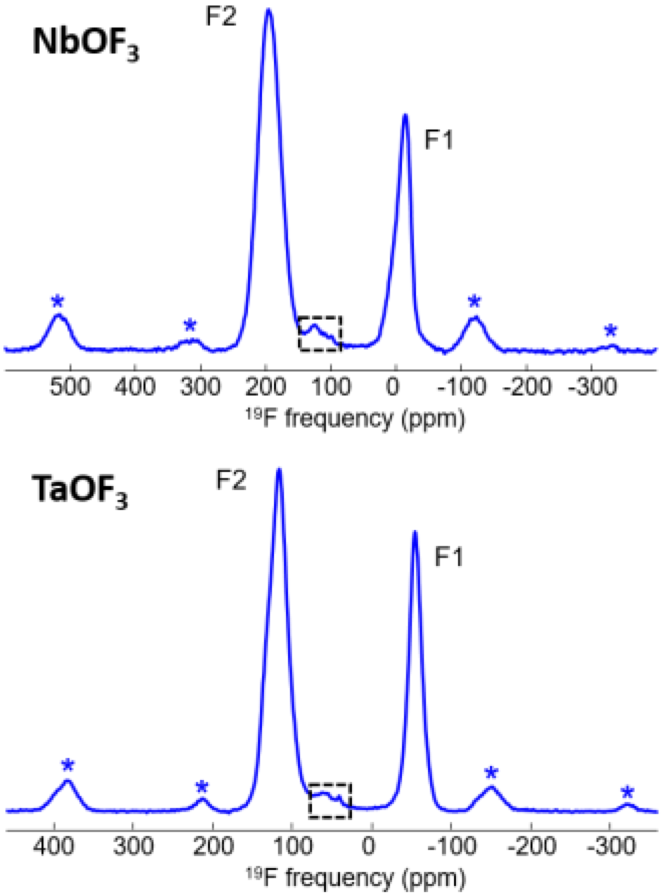

Figure 1. ^{19}F MAS NMR (4.7 T) spectra of $NbOF_3$ (60 kHz) and $TaOF_3$ (50 kHz). The stars indicate spinning sidebands. The main contributions are assigned and additional resonances, assigned to F2 site, are outlined by the dashed rectangles.

Table 1. Compound, weighted average experimental ^{19}F δ_{iso}, δ_{CSA} and η_{CSA} values ($<\delta_{iso,exp}>$, $<\delta_{CSA,exp}>$, ppm and $<\eta_{CSA,exp}>$), relative intensities (I, %) and corresponding assignments.

Compound	$<\delta_{iso,exp}>$	$<\delta_{CSA,exp}>$	$<\eta_{CSA,exp}>$	I	**Assignment**
$NbOF_3$	-8.2	-162.4	0.51	30.4	F1
	124.7	n. a.	n. a.	3.2	H-bonded F2
	195.1	-291.6	0.72	66.4	F2
$TaOF_3$	-54.9	-170.0	0.5	32.3	F1
	60.6	n. a.	n. a.	4.0	H-bonded F2
	118.1	-283.4	0.1	63.7	F2

To confirm this hypothesis, ^{1}H MAS NMR spectra of $NbOF_3$ and $TaOF_3$ were recorded (**Figure 2**) and reconstructed (**Figures S5-S6** and **Tables S5-S6**). They show similar features with two main contributions, one with δ_{iso} values ranging from 1 to 5 ppm and the other with δ_{iso} values ranging from 8 to 13 ppm (**Table 2**). Both are assigned to OH groups coordinated by Nb(Ta) atoms but the latter are H-bonded, as evidenced by their higher ^{1}H δ_{iso} value (for a X−H···Y hydrogen bond, the shorter the H···Y distance, the lower the ^{1}H magnetic shielding and the higher the ^{1}H chemical shift[97–99]). Equivalently, for an X−H···F hydrogen bond, the shorter the H···F distance, the higher the ^{19}F magnetic shielding and the lower the ^{19}F chemical shift.[100] Therefore, the existence of intermediate NMR lines with lower ^{19}F δ_{iso} (higher σ_{iso}) values is explained by the formation of O−H···F2 bonds.

The substitution of F1 atoms by OH groups leads to the general formulation $MOF_{1-x}(OH)_xF_2$. From the relative intensities of the ^{19}F MAS NMR lines, the OH substitution rates (x) are estimated to be 0.15(2) and 0.05(1) for $NbOF_3$ and $TaOF_3$, respectively (**Tables S7-S8**). Similarly to NbF_5

and TaF_5, $NbOF_3$ appears to be more hygroscopic than $TaOF_3$, resulting in a higher OH substitution rate for these niobium compounds.

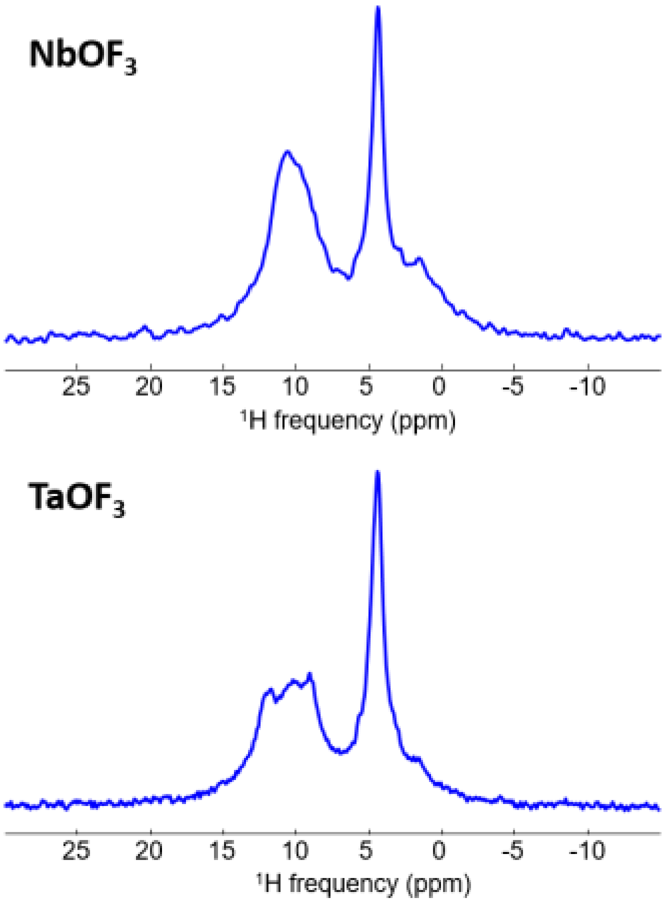

Figure 2. ^{1}H MAS NMR spectra of $NbOF_3$ (60 kHz) and $TaOF_3$ (50 kHz).

Table 2. Compound, weighted average experimental ^{1}H δ_{iso} values ($<\delta_{iso}>$, ppm) and relative intensities (I, %).

Compound	$<\delta_{iso}>$	I
$NbOF_3$	3.2	44.6
	10.3	55.4
$TaOF_3$	4.4	55.0
	11.0	45.0

4.2 Structural characterization: XRPD.

The crystal structures of $NbOF_3$ and $TaOF_3$, determined by Köhler *et al.* (*I*4/*mmm* space group (no. 139)),[15] have been revised. The recorded RT PXRD diagrams have been refined by using the Rietveld method[101] implemented in the Fullprof software.[102] For both compounds, based on ^{19}F solid-state NMR, we assumed that the terminal X2 site is fully occupied by F atoms and that the bridging X1 site has an occupancy of 0.5 O and 0.5 F and we considered isotropic displacement parameters (IDP) for all atoms. The cell parameters, atomic coordinates and IDPs are gathered in **Table 3**. The observed, calculated and intensity difference patterns and reliability factors are given as SI (**Figures S7** and **S8** for $NbOF_3$ and $TaOF_3$, respectively).

Crystal structures have been deposited via the joint CCDC/FIZ Karlsruhe deposition service. CSD[103] 2260474 and 2260475 (deposition number) contains the supplementary crystallographic data for $NbOF_3$ and $TaOF_3$, respectively. These data can be obtained free of charge from FIZ Karlsruhe via www.ccdc.cam.ac.uk/structures.

The BVS calculations[32,33] (**Table 4**), despite slightly high bond valences for Nb and Ta, indicate quite clearly an occupation of the X1 sites by O and F and a preferential occupation of the X2 sites by F. Perspective views of the unit cell of $NbOF_3$ and of *cis*- and *trans*-NbO_2F_4 octahedra are represented on **Figure 3(a)**.

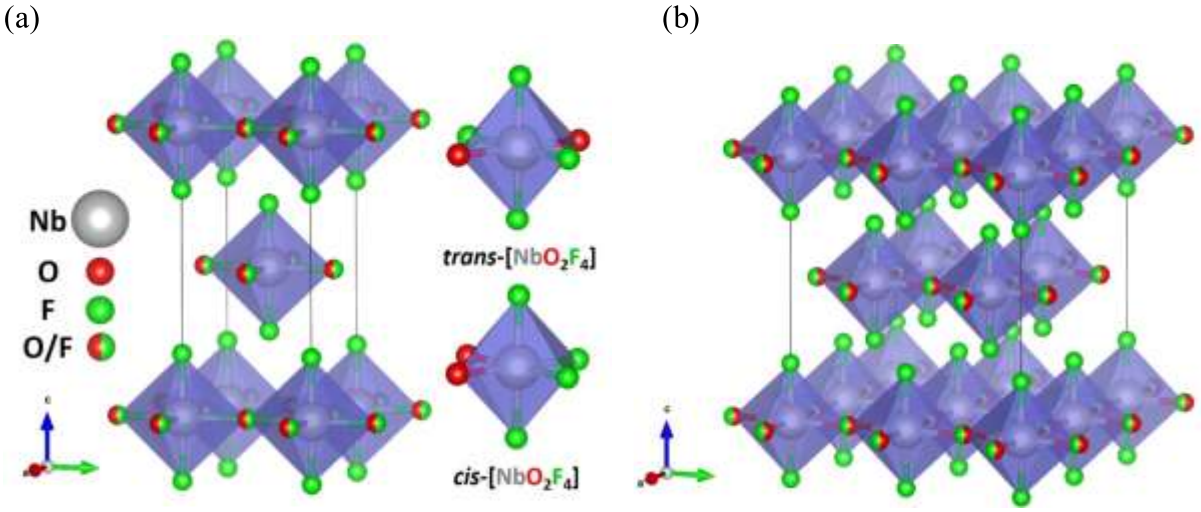

Figure 3. (a) Perspective views of the $NbOF_3$ unit cell (on the left) and of *cis*-and *trans*-NbO_2F_4 octahedra (on the right). **(b)** Perspective view of a 2×2×1 supercell. The NbO_2F_4 octahedra are displayed in purple.

Table 3. Atom, site multiplicity and Wyckoff symbol (Wyck.), site symmetry (Sym.), atomic coordinates (x, y, z), site occupancy factor (sof) and isotopic displacement parameters (U_{iso}, Å^2) in $NbOF_3$ ($a = b = 3.9739(1)$ Å, $c = 8.3612(2)$ Å) and $TaOF_3$ ($a = b = 3.9465(1)$ Å, $c = 8.4454(2)$ Å).

Atom	Wyck.	Sym.	x	y	z	sof	U_{iso}
Nb	2a	4/mmm	0	0	0	1	0.05(8)
F1	4c	mmm	1/2	0	0	0.5	0.04(8)
O1	4c	mmm	1/2	0	0	0.5	0.04(8)
F2	4e	4mm	0	0	0.2175(2)	1	0.05(8)
Ta	2a	4/mmm	0	0	0	1	0.03(15)
F1	4c	mmm	1/2	0	0	0.5	0.04(15)
O1	4c	mmm	1/2	0	0	0.5	0.04(15)
F2	4e	4mm	0	0	0.2159(4)	1	0.04(15)

Table 4. Bond valence sum values from the experimental structures (ES) and average bond valence sum values (V_i) from the APO_DFT-D3 and FO_DFT-D3 supercells of $NbOF_3$ and $TaOF_3$. The BVS values were obtained using the following values of R_0 parameters: 1.911 Å, 1.920 Å,[32] 1.87 Å and 1.88 Å[33] for Nb^{5+}/O^{2-}, Ta^{5+}/O^{2-}, Nb^{5+}/F and Ta^{5+}/F^-, respectively, and b = 0.37 Å.

$NbOF_3$	V_i^{Nb}	V_i^{O1}	V_i^{F1}	V_i^{F2}
ES	5.385	1.629	1.458	1.149
APO_DFT-D3	5.176	2.131	1.101	0.972
FO_DFT-D3	5.183	2.142	1.099	0.971
$TaOF_3$	$\mathbf{V_i^{Ta}}$	$\mathbf{V_i^{O1}}$	$\mathbf{V_i^{F1}}$	$\mathbf{V_i^{F2}}$
ES	5.617	1.732	1.554	1.165
APO_DFT-D3	5.350	2.227	1.186	0.968
FO_DFT-D3	5.258	2.181	1.130	0.973

4.3 O/F correlated disorder.

As mentioned in the introduction, O/F correlated disorder has been previously highlighted in $Nb_3O_5F_5$,[30] NbO_2F[29,31] and TaO_2F[25,31] resulting in one-dimensional O/F-ordered strings of atoms and out-of-center displacement of metal cations. For $NbOF_3$, the presence of O/F correlated disorder in the $_\infty(MOF_3)$ layers, along <100> and <010> directions, has been predicted.[30] From our experimental results, in both MOF_3 compounds, the X1 site has an occupancy of 0.5 O and 0.5 F and the X2 site occupied only by F leading to either *cis*- or *trans*-MO_2F_4 octahedra (**Figure 3(a)**). The former octahedral units are more favored, particularly when the cation is a d^0 transition metal. Indeed, having anions with similar Pearson hardness near each other maximizes the π-hybridization in the M-anion bonds by allowing atomic relaxations toward characteristic bond lengths (*i.e.*, cation displacements toward the less electronegative anion).[2] This results in one-dimensional –F–M–O–M– chains along <100> and <010> directions.

4.4 Possible models for $NbOF_3$ and $TaOF_3$ using 2×2×1 supercells

Considering a 2×2×1 supercell (**Figure 3(b)**), there are only three ways to construct a $_{\infty}(MOF_3)$ layer with *cis*-MO_2F_4 octahedra corner-connected by two O atoms and two F atoms (**Figure 4(a)**). Since each supercell consists of two stacked $_{\infty}(MOF_3)$ layers and excluding all symmetry equivalent combinations, ten different 2×2×1 supercells have been built (**Figure 4(b)**). These ten models were then geometry optimized. The structural characteristics of the ten non-optimized, APO_DFT-D3 and FO_DFT-D3 optimized supercells, for $NbOF_3$ and $TaOF_3$, are summarized in **Tables 5** and **6** (details for each model are given as SI in **Figure S9** and **Tables S9–S22**). For $NbOF_3$ and $TaOF_3$, each of the ten APO_DFT-D3 and FO_DFT-D3 models exhibits similar structural characteristics.

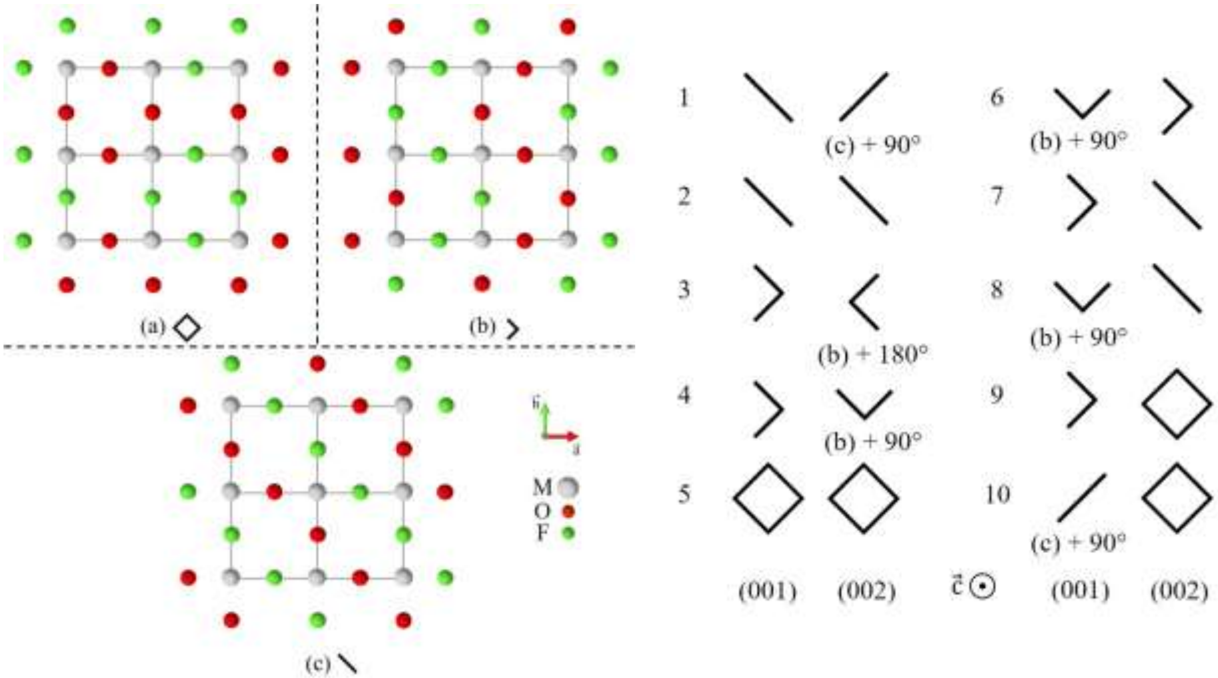

Figure 4. (Left) Representation of the three ways to construct a $_\infty$(MOF$_3$) layer with *cis*-MO$_2$F$_4$ octahedra corner-connected by two O atoms and two F atoms, labeled as (a) diamond (◊), (b) zigzag (>) and (c) diagonal (\). (Right) Illustration of two successive ($\vec{a},\vec{b}$) planes, (001) and (002), for each of the ten constructed models. The rotational operation around $\vec{c}$ involved for five of the models are indicated.

Table 5. Average cell parameters (*a*, *b* and *c*, Å), average supercell volume (Å^3), average M–O1, M–F1 and M–F2 bond lengths (Å) from the ten non-optimized (ES), and APO_DFT-D3 and FO_DFT-D3 optimized supercells of $NbOF_3$ and $TaOF_3$.

Supercell	***a***	***b***	***c***	***V***	**M–O1**	**M–F1**	**M–F2**
	$NbOF_3$						
ES	7.948	7.948	8.361	528.2	1.987	1.987	1.819
APO_DFT-D3	7.948	7.948	8.361	528.2	1.888	2.092	1.881
FO_DFT-D3	7.945	7.944	8.266	521.7	1.886	2.093	1.881
	$TaOF_3$						
ES	7.893	7.893	8.445	526.1	1.973	1.973	1.823
APO_DFT-D3	7.893	7.893	8.445	526.1	1.880	2.073	1.892
FO_DFT-D3	7.945	7.945	8.351	527.1	1.888	2.091	1.890

When the supercells are fully optimized, the cell parameters *a* and *b* are more or less constant for $NbOF_3$ and increase for $TaOF_3$. For both, *c* decreases. The cell volume slightly decreases for $NbOF_3$ (1.2 %) and remains almost constant for $TaOF_3$ (+ 0.2%) which seems to demonstrate the effectiveness of the dispersion correction. We observe, after APO and FO, atomic relaxations towards characteristic bond lengths, *i.e.*, metal displacements towards oxygen, the least electronegative atom, as shown by the decrease of the average M–O1 (increase of the average M–F1) bond lengths (~ 0.1 Å, **Table 5**) and the increase of the average O1–M–O1 (decrease of the average F1–M–F1) angles (~ 6°, **Table 6** and **Figure 5**). The M–F2 bond lengths increase (~ 0.06 Å, **Table 5**) and the F2–M–F2 angles decrease (from 180° to ~ 163°, **Table 6** and **Figure 5**). From the decrease of the F2–M–F2 angles, it can be estimated that, in the average structure, the M–F2 bond lengths are underestimated by about 0.02 Å. $_{\infty}$(MOF$_3$) layers are then getting closer in the optimized supercells since the decrease in angle values does not compensate for the increase in bond lengths. This is even more pronounced for the full optimized supercells for which the cell parameters *c* are smaller.

After optimization, the values for bond lengths and bond angles not only deviate from the average values determined by diffraction but are, as expected in disordered compounds, distributed.

Table 6. Average X−M−X Angles (°) between Adjacent (X1−M−X1) and Opposite (F2−M−F2)) M−X Bonds and Average M–O1–M and M–F1–M angles (°) of the 10 APO_DFT-D3 and 10 FO_DFT-D3 optimized supercells of NbOF$_3$ and TaOF$_3$.

Supercells	F1–M–F1-	O1–M–O1	F2–M–F2	M–O1–M	M–F1–M
	NbOF$_3$				
APO_DFT-D3	83.6	96.5	162.7	176.9	176.7
FO_DFT-D3	83.5	96.6	162.8	177.0	176.6
	TaOF$_3$				
APO_DFT-D3	83.2	96.6	163.7	176.8	176.2
FO_DFT-D3	83.4	96.6	163.2	176.9	176.8

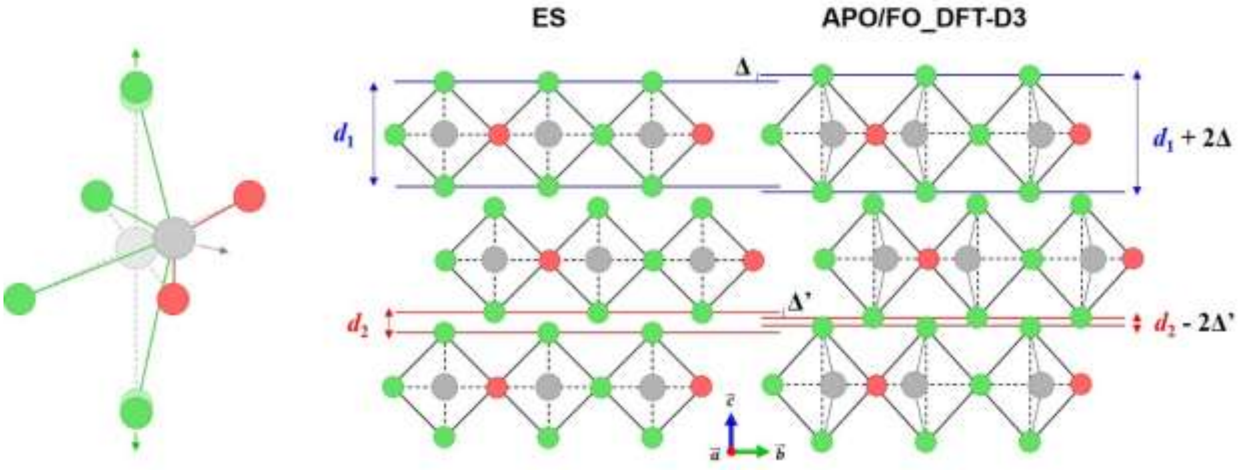

Figure 5. Illustration of the optimization effect on the MO_2F_4 octahedra (left) and on the thickness d_1 of the $_\infty(MOF_3)$ layers as well as the distance d_2 between them (right). M, O and F are represented in grey, red and green, respectively.

4.5 $\delta_{iso} = \sigma_{ref} - a\, \sigma_{iso}$ equations for ^{19}F from NbF_5 and TaF_5

The equations used to convert the ^{19}F σ_{iso} values into δ_{iso} values were established from the two isomorph binary pentafluorides NbF_5 and TaF_5. The calculations were done using the same conditions as for $NbOF_3$ and $TaOF_3$, *i.e.*, on APO and FO structures, both including DFT-D3, for consistency and because NbF_5 and TaF_5 consist of tetrameric structural units $[M_4F_{20}]$ (M = Nb, Ta), built up from MF_6 octahedra linked to each other by corners, in a *cis*-configuration, and held together by vdW interactions. They seem perfectly suitable for establishing such predictive equations since they present several F crystallographic sites, including, like $NbOF_3$ and $TaOF_3$, bridging and terminal F atoms. The linear regressions between the calculated σ_{iso} values and experimental δ_{iso} values[83] of ^{19}F (**Table S23**) are reported in **Figure 6**. For NbF_5, the equations are: δ_{iso} (ppm) = −1.031(6) σ_{iso} + 97.3(8) and δ_{iso} (ppm) = −1.034(17) σ_{iso} + 96.4(2.3) for APO_DFT-D3 and FO_DFT-D3, respectively. For TaF_5 the equations are: δ_{iso} (ppm) = −0.968(15) σ_{iso} + 107.4(1.3) and δ_{iso} (ppm) = −0.968(7) σ_{iso} + 107.9(6) for APO_DFT-D3 and FO_DFT-D3, respectively. The slopes of the TaF_5 linear regressions, established using σ_{iso} values calculated with the VASP code, are closer to the theoretical -1 value in comparison to those (~ -0.78 for APO structures) established using σ_{iso} values calculated with the CASTEP code.[83] In contrast, the slopes of the NbF_5 linear regressions remain close whatever the code used to calculate the σ_{iso} values.

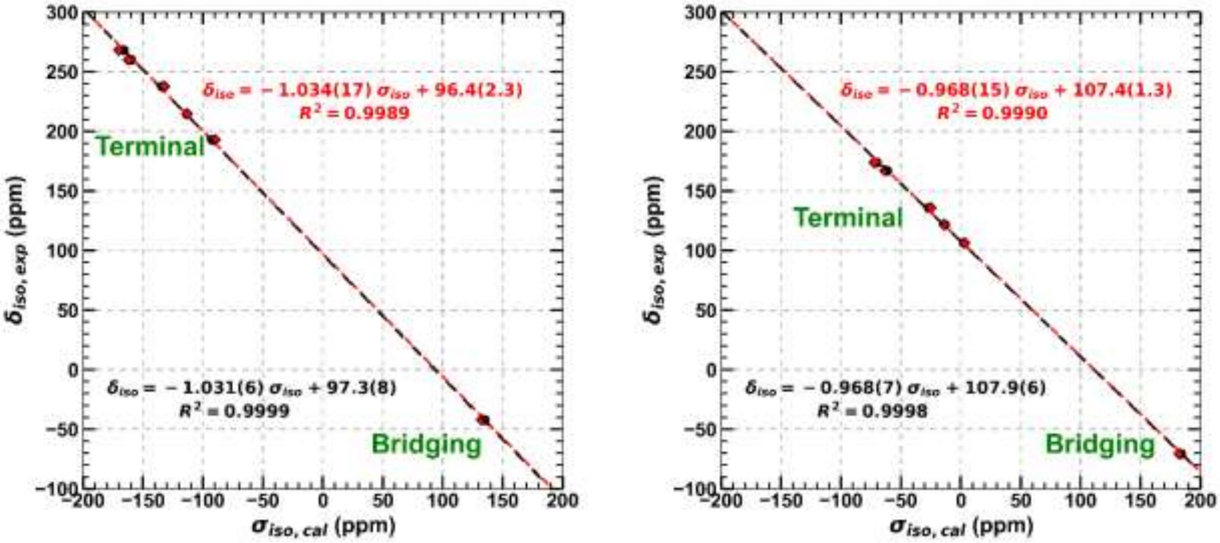

Figure 6. Calculated ^{19}F σ_{iso} values as function of the experimental ^{19}F δ_{iso} values for NbF_5 (left) and TaF_5 (right). The red squares and the black dots correspond respectively to the values calculated from the FO_DFT-D3 and APO_DFT-D3 structures. The dash red and black lines represent the linear regressions when considering the calculated σ_{iso} values from the FO_DFT-D3 and APO_DFT-D3 structures, respectively. Their equations are given in red and black, respectively.

4.6 Theoretical ^{19}F solid state NMR spectra of $NbOF_3$ and $TaOF_3$

The structural features of the APO_DFT-D3 and FO_DFT-D3 models being similar for each compound, consistently, the calculated ^{19}F σ_{iso}, σ_{CSA} and η_{CSA} values are similar as well (**Tables S24–S35**). Using the linear regression equations above (**Figure 6**), the calculated ^{19}F σ_{iso} values were converted into δ_{iso} values and the average δ_{iso}, σ_{CSA} and η_{CSA} values from each model are gathered in **Tables 7 and 8**. The δ_{iso} values of the terminal F2 atoms decrease linearly as the F2–M bond lengths increase (**Figure S10**).

For both compounds, and in agreement with more intense spinning sidebands, the calculated σ_{CSA} values are higher for F2 atoms compared to F1 atoms. The η_{CSA} values show good agreement for both F1 and F2 atoms in $TaOF_3$, and a less satisfying agreement for F2 atoms in $NbOF_3$ (**Tables 1**, **7** and **8**). For $TaOF_3$, the agreement between calculated and experimental average ^{19}F δ_{iso} values is almost perfect for both F1 and F2 atoms. In contrast, for $NbOF_3$, this agreement is less satisfying for the F2 atoms. Furthermore, the dispersion of the calculated δ_{iso} values for each model is consistent with the widths of the NMR signals (**Tables S1-S4**, and **S24, S27, S30 and S33**). Therefore, since there is no significant difference between the total energy of each model (**Table S10**), there is no reason to rule out any particular model and we assume that they all contribute equally to the structural modeling of MOF_3. Theoretical ^{19}F NMR spectra were then plotted considering the 240 (80 F1 and 160 F2) calculated δ_{iso} values. These spectra being similar we present only those from the APO_DFT-D3 models (**Figure 7**). The agreement between the experimental and theoretical spectra is excellent for $TaOF_3$, but less satisfactory for $NbOF_3$ in particular for the NMR line corresponding to the F2 atoms (**Table 9**). Assuming that it is related to the higher OH group content in $NbOF_3$, we have studied the effect of the substitution of F1 atoms by OH groups on the structure and on the NMR parameters.

Table 7. Average calculated ^{19}F δ_{iso} (ppm), σ_{CSA} (ppm) and η_{CSA} values for each APO_DFT-D3 and FO_DFT-D3 optimized supercells of $NbOF_3$. The equations used to convert the calculated ^{19}F σ_{iso} values into calculated ^{19}F δ_{iso} values are those established from the APO_DFT-D3 and FO_DFT-D3 structures of NbF_5 (**Figure 6**).

	APO_DFT-D3						**FO_DFT-D3**					
	F1			**F2**			**F1**			**F2**		
Model	δ_{iso}	σ_{CSA}	η_{CSA}	δ_{iso}	σ_{CSA}	η_{CSA}	δ_{iso}	σ_{CSA}	η_{CSA}	δ_{iso}	σ_{CSA}	η_{CSA}
1	-17.6	147.6	0.71	213.9	330.7	0.12	-17.9	147.7	0.71	212.6	329.8	0.12
2	-17.5	143.3	0.91	209.1	330.1	0.03	-16.3	144.9	0.90	207.7	328.8	0.02
3	-14.0	141.7	0.79	211.5	327.7	0.29	-12.6	142.3	0.80	210.0	326.2	0.32
4	-18.1	139.9	0.79	215.5	331.4	0.12	-18.7	139.2	0.80	213.6	330.1	0.12
5	-7.0	151.2	0.91	212.8	332.2	0.06	-7.4	149.9	0.90	210.0	330	0.07
6	-17.3	141.4	0.85	211.0	331	0.08	-17.2	141.6	0.84	208.8	329.2	0.08
7	-17.4	144.9	0.79	211.6	330.7	0.08	-17.2	145.2	0.79	209.9	329.4	0.08
8	-18.0	143.7	0.73	215.6	331.0	0.11	-18.7	142.9	0.74	213.9	329.9	0.10
9	-8.6	147.2	0.79	210.7	327.3	0.25	-4.4	150.6	0.74	208.0	324	0.40
10	-12.2	150.6	0.78	213.7	331.4	0.08	-12.8	149.8	0.79	211.6	329.8	0.08

Table 8. Average calculated ^{19}F δ_{iso}, σ_{CSA} (ppm) and η_{CSA} values for each APO_DFT-D3 and FO_DFT-D3 optimized supercells of $TaOF_3$. The equations used to convert the calculated ^{19}F σ_{iso} values into calculated ^{19}F δ_{iso} values are those established from the APO_DFT-D3 and FO_DFT-D3 structures of TaF_5 (**Figure 6**).

	APO_DFT-D3						**FO_DFT-D3**					
	F1			**F2**			**F1**			**F2**		
Model	$\delta_{iso,cal}$	σ_{CSA}	η_{CSA}	$\delta_{iso,cal}$	σ_{CSA}	η_{CSA}	$\delta_{iso,cal}$	σ_{CSA}	η_{CSA}	$\delta_{iso,cal}$	σ_{CSA}	η_{CSA}
1	-54.7	120.7	0.74	115.5	268.1	0.11	-53.8	123.2	0.75	119.6	272.6	0.11
2	-54.7	123.4	0.73	112.9	267.8	0.02	-52.8	125.4	0.79	116.8	272.4	0.00
3	-55.2	115	0.81	115.9	268.9	0.08	-54.2	117.7	0.84	119.2	272.7	0.08
4	-55.3	114.8	0.77	117.0	269	0.11	-54.7	117.7	0.79	120.3	272.9	0.11
5	-49.7	122.3	0.78	115.4	269.6	0.04	-48.6	123.5	0.87	118.1	272.8	0.05
6	-55.2	119.4	0.7	114.3	268.7	0.05	-53.8	120.8	0.78	117.6	272.6	0.05
7	-54.9	119.7	0.76	114.5	268.4	0.06	-53.5	122.3	0.78	118.1	272.6	0.06
8	-54.9	114.9	0.83	116.9	268.5	0.10	-54.3	117.8	0.83	120.5	272.7	0.10
9	-52.4	119	0.79	115.8	269.3	0.07	-51.4	121.4	0.83	118.8	272.8	0.07
10	-52.1	119.4	0.83	115.8	268.8	0.07	-51.0	122.8	0.84	119.0	272.7	0.07

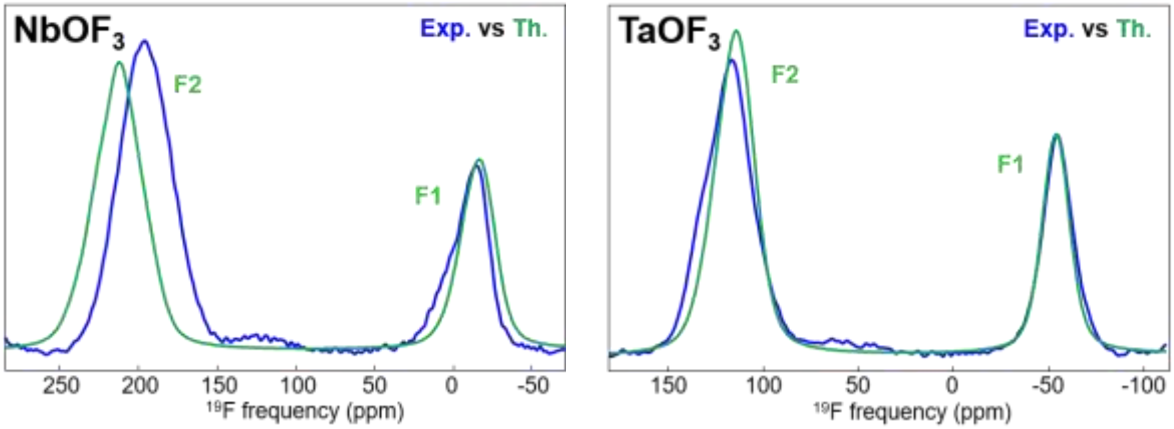

Figure 7. Experimental (blue) and theoretical (green) ^{19}F NMR spectra of NbOF$_3$ and TaOF$_3$. The experimental spectra were processed by using the TOP procedure.[71] The theoretical spectra were built using the calculated ^{19}F δ_{iso} values from the APO_DFT-D3 models.

Table 9. ^{19}F Experimental weighted average $\delta_{iso,exp}$, δ_{CSA} and η_{CSA} values, and calculated average $\delta_{iso,cal}$, σ_{CSA} and η_{CSA} values from APO_DFT-D3 and FO_DFT-D3 models, of F1 and F2 atoms in NbOF$_3$ and TaOF$_3$ (ppm).

	Experimental data			APO_DFT-D3			FO_DFT-D3		
F atoms	$\delta_{iso,exp}$	δ_{CSA}	η_{CSA}	$\delta_{iso,cal}$	σ_{CSA}	η_{CSA}	$\delta_{iso,cal}$	σ_{CSA}	η_{CSA}
NbOF$_3$									
F1	-8.2	-162.4	0.51	-14.8	145.1	0.81	-14.3	145.4	0.80
F2	194.3	-291.6	0.72	212.5	330.4	0.12	210.6	328.7	0.14
TaOF$_3$									
F1	-54.6	-170	0.5	-53.9	118.9	0.77	-52.8	121.3	0.81
F2	118.2	-283.4	0.1	115.4	268.7	0.07	118.8	272.7	0.07

4.7 Modeling hydroxylated $NbOF_3$.

New supercells $NbO1F1_{1-x}(OH)1_xF2_2$ were then built with two different OH substitution rates, x = 1/8 and x = 1/4. For each of the ten models, the substitution of one or two F1 atoms by OH groups was performed using the "Supercell" program[104] and led to multiple possible configurations. Testing all possible configurations for all models is beyond the limits of our computational hardware. Therefore, only the supercell with the lowest coulomb energy was chosen for each $NbOF_3$ model and substitution rate. The atomic positions of the selected supercells were then optimized and the structural characteristics are gathered as SI in **Tables S36-S43**. The NMR parameters are then calculated and the ^{19}F σ_{iso} converted into ^{19}F δ_{iso} values by using the linear regression equations established on NbF_5 (**Tables S44-S49**). Average values are gathered in **Table 10** and the two new theoretical ^{19}F NMR spectra are presented in **Figure 8**. The agreement between experimental and theoretical spectra is improved. Substituting F1 atoms by OH groups results in a decrease of the average F2 δ_{iso} value and thus of the gap between the calculated and experimental F2 resonances, without significant variation of the average F1 δ_{iso} values. Moreover, some F2 atoms have significantly lower δ_{iso} values (**Figure 9** and **Table 10**) and they are distinguishable when plotted against F2–M bond lengths (**Figure S11**). A combined analysis of the structural data and calculated ^1H and ^{19}F δ_{iso} values shows that each OH groups is involved either in one strong O–H···F bond or four O–H···F weak bonds or contacts (**Tables 11, S50** and **S51**). Usually, O–H···F contacts with angles (°) larger than 115° and H···F distances (Å) smaller than the sum of H (1.20 Å) and F (1.47 Å) van der Waals radii are considered as H-bonds. The ^{19}F δ_{iso} values of the F2 atoms involved in O–H···F weak bonds or contacts are only slightly lower than those of the remaining F2 atoms and contribute to the decrease of the δ_{iso} value of the main F2 resonance. The calculated ^1H δ_{iso} values of the H atoms forming weak O–H···F bonds or contact are only slightly less than to those of H atoms forming a unique and strong H bond. Overall, the ^{1}H calculated δ_{iso} values are close to those of the NMR line assigned to H-bonded OH (**Table 2**). The experimental spectrum shows a second contribution assigned to non H-bonded OH. Indeed, at room temperature and in the course of time, the rotational movement of OH groups enables the formation and breaking of these H-bonds, whereas these effects cannot not be captured by the inherently static DFT optimized structure at 0 K.

Table 10. Weighted average ^{19}F experimental δ_{iso} values (in italic) and average theoretical δ_{iso} values for F2, strongly H-bonded F2 and F1 atoms ($<\delta_{iso}>$, ppm) and corresponding relative intensities (*I*, %) from the studied sample and $NbOF_{1-x}(OH)_xF_2$ models.

	$<\delta_{iso}>$			***I***		
	F2	H bonded F2	F1	F2	H bonded F2	F1
$NbOF_{2.85}(OH)_{0.15}$	*194.3*	*120.3*	*-8.2*	*67.2*	*2.9*	*29.9*
$NbOF_3$	212.5	n. a.	-14.8	66.7	n. a.	33.3
$NbOF_{0.875}(OH)_{0.125}F_2$	205.1	112.6	-14.8	67.8	1.8	30.4
$NbOF_{0.75}(OH)_{0.25}F_2$	199.9	97.2	-15.9	67.3	5.4	27.3

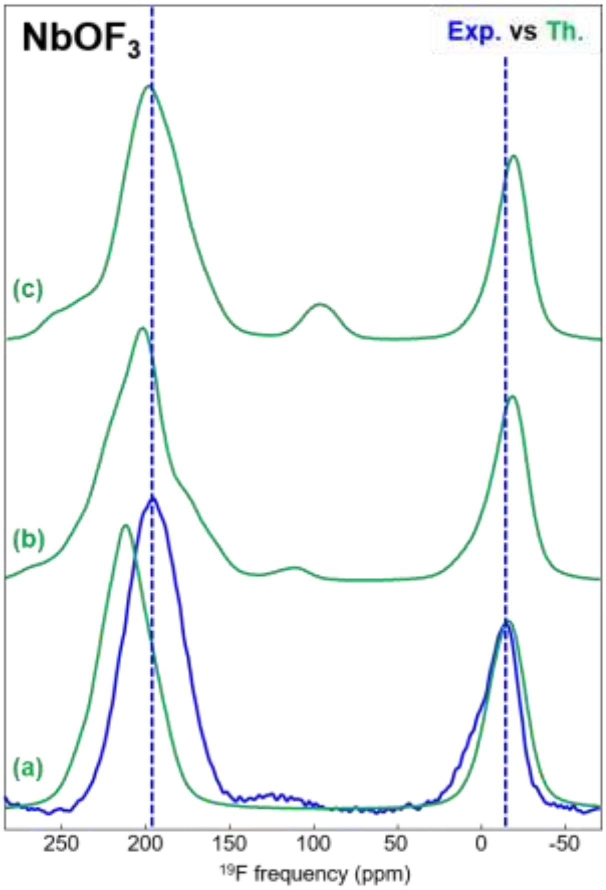

Figure 8. Experimental (blue) and theoretical (green) ^{19}F NMR spectra of $NbOF_3$ (a), $NbOF_{0.875}(OH)_{0.125}F_2$ (b) and $NbOF_{0.75}(OH)_{0.25}F_2$ (c). The experimental spectrum was processed by using the TOP procedure.[71] The theoretical spectra are constructed with the calculated ^{19}F δ_{iso} from the APO_DFT-D3 models.

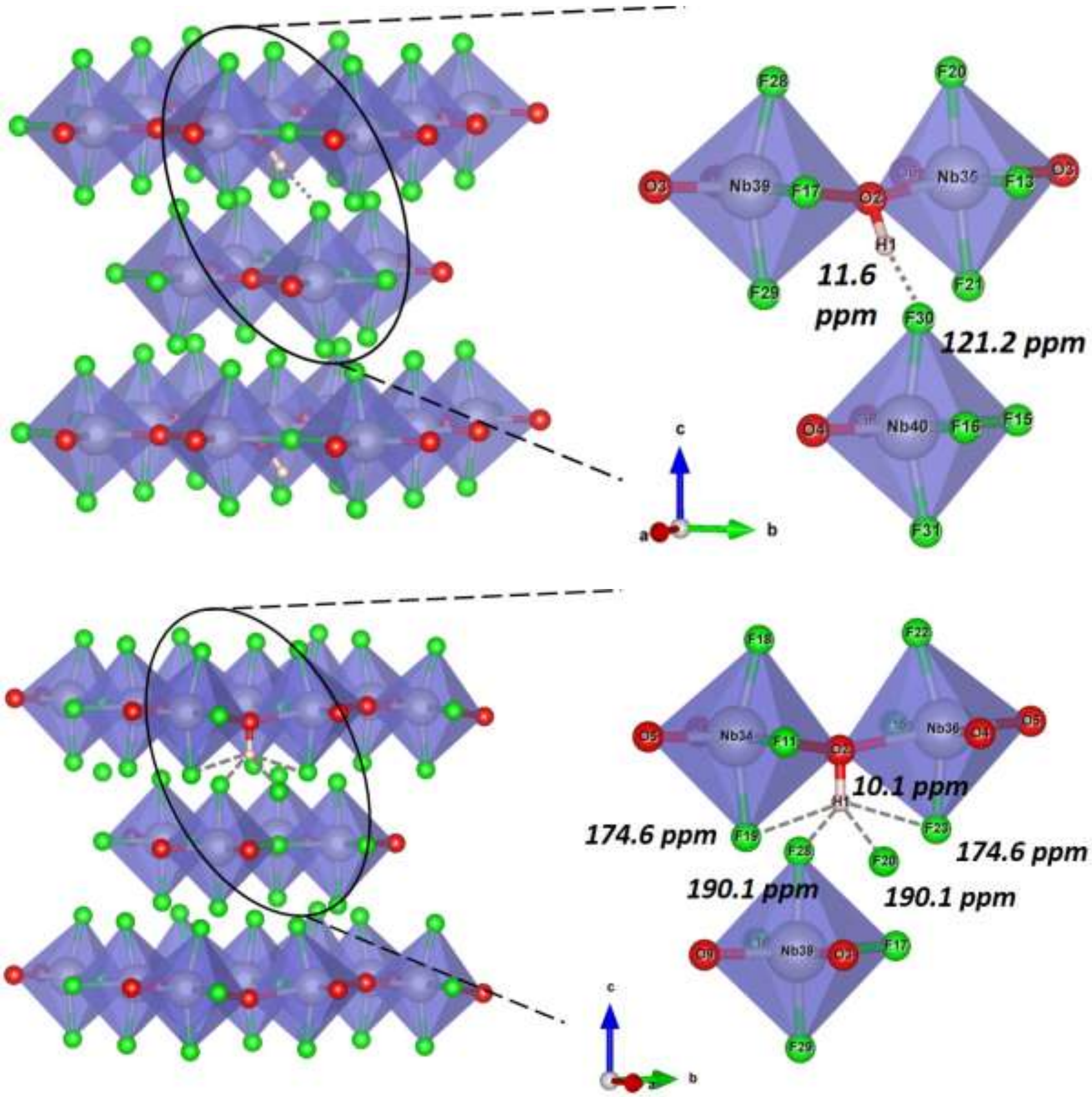

Figure 9. Perspective view of the APO_DFT-D3 models 10 (top left) and 1 (bottom left) from $NbOF_{0.875}(OH)_{0.125}F_2$. Enlargement showing a strong O–H···F bond (top right) and O–H···F contacts (bottom right). ^1H and ^{19}F δ_{iso} values are indicated. Nb, O, F and H atoms are represented in grey, red, green and white, respectively. The MX_6 octahedra are represented in purple.

Table 11. Geometries of the O−H···F contacts (average H−O bond length (Å), H···F distance (Å) and O–H···F angle (°)) and corresponding calculated ^{1}H and ^{19}F δ_{iso} values (ppm) for the ten supercells $NbOF_{0.875}(OH)_{0.125}F_2$ and $NbOF_{0.75}(OH)_{0.25}F_2$.

H−O	H···F	O−H···F	^{1}H δ_{iso}	^{19}F δ_{iso}
$NbOF_{0.875}(OH)_{0.125}F_2$				
0.999	1.662	174.1	11.8	112.6
0.985	2.184	111.6	10.0	182.2
$NbOF_{0.75}(OH)_{0.25}F_2$				
1.000	1.661	172.1	12.0	97.1
0.988	2.126	113.3	10.5	182.2

5. Conclusion

The average crystal structures of $NbOF_3$ and $TaOF_3$, especially the occupancy rates of the anion crystallographic sites based on a correct assignment of the ^{19}F NMR resonances, have been revised. The non-bridging site is fully occupied by F while the bridging site has an occupancy of 0.5 O and 0.5 F. The structure consists of stacked $_{\infty}(MOF_3)$ layers along the $\vec{c}$ direction, formed by MO_2F_4 octahedra, corner-connected by two F and two O atoms. An O/F correlated disorder is then expected since *cis*-MO_2F_4 octahedra are favored. Ten different 2×2×1 supercells per compound, fulfilling these characteristics, were built and DFT optimized, and the ^{19}F isotropic chemical shift values were determined. The agreement between the experimental and theoretical ^{19}F spectra is excellent for $TaOF_3$ but less satisfactory for $NbOF_3$ in relation with its higher OH group content. New supercells involving OH groups were then generated. A good agreement between the experimental and theoretical ^{19}F and ^{1}H calculated δ_{iso} values is obtained for the supercells with the composition closest to that estimated, *i.e.*, $NbOF_{2.85}(OH)_{0.15}$. All these results confirm the O/F correlated disorder and show that the ten possible 2×2×1 supercells present a good structural model of $NbOF_3$ and $TaOF_3$. The short-range structures deviate markedly from the average crystal structures to accommodate the different, by ~ 0.2 Å, M−O and M−F bond lengths. The building unit of MOF_3, the *cis*-MO_2F_4 octahedra, are especially distorted with average angle values between adjacent and opposite M−X bonds away from the values of the average structure. The values for bond lengths and bond angles not only deviate from the average values determined by diffraction but are, as expected in disordered compounds, distributed. Finally, the structural modeling of hydroxylated $NbOF_3$ highlights that each H atom is either strongly H bonded to one F2 atom or in contact with four F2 atoms. This study proves the efficiency of combining theoretical calculations and solid-state NMR to model O/F correlated disorder in oxyfluorides as well as their hydroxylation.

ASSOCIATED CONTENT

Supporting Information. The Supporting Information is available free of charge on the ACS Publications website at DOI:

^{19}F and ^{1}H MAS NMR spectra and their fits; determination of the OH substitution rate in $NbOF_3$ and $TaOF_3$; Rietveld refinements; $NbOF_3$, $TaOF_3$ and hydroxylated $NbOF_3$ structural features; new NbF_5 and TaF_5 correlations ^{19}F σ_{iso} vs δ_{iso} established with VASP; $NbOF_3$, $TaOF_3$ and hydroxylated $NbOF_3$ calculated δ_{iso}, σ_{CSA} and η_{CSA} values; geometries of the O−H···F contacts and calculated δ_{iso} values in hydroxylated $NbOF_3$. (SI.pdf)

CIF files for ES structures of $NbOF_3$ and $TaOF_3$, the 10 APO_DFT-D3 and the 10 FO_DFT-D3 models of $NbOF_3$ and $TaOF_3$, the 10 APO_DFT-D3 models of $NbOF_{0.875}(OH)_{0.125}F_2$ and $NbOF_{0.75}(OH)_{0.25}F_2$ (CIF_files.zip).

AUTHOR INFORMATION

Corresponding Authors

*E-mail: Ouail.Zakary@univ-lemans.fr.

*E-mail: Monique.Body@univ-lemans.fr

ORCID

Ouail Zakary: 0000-0002-7793-3306

Monique Body: 0000-0002-5895-3731

Thibault Charpentier: 0000-0002-3034-1389

Vincent Sarou-Kanian: 0000-0001-9611-8377

Christophe Legein: 0000-0001-7426-8817

Author Contributions

The manuscript was written through contributions of all authors. All authors have given approval to the final version of the manuscript.

Notes

The authors declare no competing financial interest.

ACKNOWLEDGMENT

The authors acknowledge Cyrille Galven (IMMM – UMR 6283 CNRS, Le Mans Université) for his support with the synthesis.

REFERENCES

(1) Kageyama, H.; Hayashi, K.; Maeda, K.; Attfield, J. P.; Hiroi, Z.; Rondinelli, J. M.; Poeppelmeier, K. R. Expanding Frontiers in Materials Chemistry and Physics with Multiple Anions. *Nat Commun* **2018**, *9* (1), 772. https://doi.org/10.1038/s41467-018-02838-4.

(2) Harada, J. K.; Charles, N.; Poeppelmeier, K. R.; Rondinelli, J. M. Heteroanionic Materials by Design: Progress Toward Targeted Properties. *Adv. Mater.* **2019**, *31* (19), 1805295. https://doi.org/10.1002/adma.201805295.

(3) Agulyansky, A. *Chemistry of Tantalum and Niobium Fluoride Compounds*; Elsevier, 2004. https://doi.org/10.1016/B978-0-444-51604-6.X5000-9.

(4) Frevel, L. K.; Rinn, H. W. The Crystal Structure of NbO_2F and TaO_2F. *Acta Cryst* **1956**, *9* (8), 626–627. https://doi.org/10.1107/S0365110X56001728.

(5) Andersson, S.; Åström, A.; Issidorides, C.; Kallner, A. The Thermal Decomposition of NbO_2F. *Acta Chem. Scand.* **1965**, *19*, 2136–2138. https://doi.org/10.3891/acta.chem.scand.19-2136.

(6) Carlson, S.; Larsson, A.-K.; Rohrer, F. E. High-Pressure Transformations of NbO_2F. *Acta Crystallogr B Struct Sci* **2000**, *56* (2), 189–196. https://doi.org/10.1107/S0108768199015311.

(7) Reddy, M. V.; Madhavi, S.; Subba Rao, G. V.; Chowdari, B. V. R. Metal Oxyfluorides $TiOF_2$ and NbO_2F as Anodes for Li-Ion Batteries. *Journal of Power Sources* **2006**, *162* (2), 1312–1321. https://doi.org/10.1016/j.jpowsour.2006.08.020.

(8) Jahnberg, L.; Andersson, S.; Fischer, P.; Stoll, E.; Eriksson, G.; Blinc, R.; Paušak, S.; Ehrenberg, L.; Dumanović, J. Studies on Pentavalent Tantalum Oxide Fluorides and the Thermal

Decomposition of TaO_2F. *Acta Chem. Scand.* **1967**, *21*, 615–619. https://doi.org/10.3891/acta.chem.scand.21-0615.

(9) Andersson, S.; Åström, A.; Weedon, B. C. L. Phase Analysis Studies on Niobium Oxide Fluorides. *Acta Chem. Scand.* **1964**, *18*, 2233–2236. https://doi.org/10.3891/acta.chem.scand.18-2233.

(10) Andersson, S.; Åsbrink, S.; Reistad, T.; Sparrow, D. R. The Crystal Structure of Nb_3O_7F. *Acta Chem. Scand.* **1964**, *18*, 2339–2344. https://doi.org/10.3891/acta.chem.scand.18-2339.

(11) Vlasse, M.; Morilière, C.; Chaminade, J.-P.; Pouchard, M. Structure cristalline de l'oxyfluorure de tantale Ta_3O_7F α. *Bull. Soc. Fr. Minéral. Cristallogr.* **1975**, *98* (6), 325–330. https://doi.org/10.3406/bulmi.1975.7012.

(12) Andersson, S.; Nord, S.; Sjöberg, B.; Mellander, O.; Hinton, M. Two New Niobium Oxide Fluorides Formed at High Temperature. *Acta Chem. Scand.* **1965**, *19*, 1401–1404. https://doi.org/10.3891/acta.chem.scand.19-1401.

(13) Åström, A. The Crystal Structures of $Nb_{31}O_{77}F$ and $Nb_{17}O_{42}F$. *Acta Chem. Scand.* **1966**, *20*, 969–982. https://doi.org/10.3891/acta.chem.scand.20-0969.

(14) Cordier, S.; Roisnel, T.; Poulain, M. Synthesis and Characterization of the Novel $Nb_3O_5F_5$ Niobium Oxyfluoride: The Term N=3 of the $Nb_nO_{2n-1}F_{n+2}$ Series. *Journal of Solid State Chemistry* **2004**, *177* (9), 3119–3126. https://doi.org/10.1016/j.jssc.2004.05.032.

(15) Köhler, J.; Simon, A.; Van Wüllen, L.; Cordier, S.; Roisnel, T.; Poulain, M.; Somer, M. Structures and Properties of $NbOF_3$ and $TaOF_3$ — With a Remark to the O/F Ordering in the SnF_4

Type Structure. *Z. Anorg. Allg. Chem.* **2002**, *628* (12), 2683–2690. https://doi.org/10.1002/1521-3749(200212)628:12<2683::AID-ZAAC2683>3.0.CO;2-E.

(16) Murase, T.; Irie, H.; Hashimoto, K. Ag^+-Inserted NbO_2F as a Novel Photocatalyst. *J. Phys. Chem. B* **2005**, *109* (28), 13420–13423. https://doi.org/10.1021/jp050423t.

(17) Lange, M. A.; Khan, I.; Dören, R.; Ashraf, M.; Qurashi, A.; Prädel, L.; Panthöfer, M.; von der Au, M.; Cossmer, A.; Pfeifer, J.; Meermann, B.; Mondeshki, M.; Tahir, M. N.; Tremel, W. High-Speed Solid State Fluorination of Nb_2O_5 Yields NbO_2F and Nb_3O_7F with Photocatalytic Activity for Oxygen Evolution from Water. *Dalton Trans.* **2021**, *50* (19), 6528–6538. https://doi.org/10.1039/D1DT00533B.

(18) Xu, L.; Gong, H.; Deng, L.; Long, F.; Gu, Y.; Guan, J. Complex-Mediated Synthesis of Tantalum Oxyfluoride Hierarchical Nanostructures for Highly Efficient Photocatalytic Hydrogen Evolution. *ACS Appl. Mater. Interfaces* **2016**, *8* (14), 9395–9404. https://doi.org/10.1021/acsami.6b02622.

(19) Lange, M. A.; Khan, I.; Opitz, P.; Hartmann, J.; Ashraf, M.; Qurashi, A.; Prädel, L.; Panthöfer, M.; Cossmer, A.; Pfeifer, J.; Simon, F.; von der Au, M.; Meermann, B.; Mondeshki, M.; Tahir, M. N.; Tremel, W. A Generalized Method for High-Speed Fluorination of Metal Oxides by Spark Plasma Sintering Yields Ta_3O_7F and TaO_2F with High Photocatalytic Activity for Oxygen Evolution from Water. *Adv. Mater.* **2021**, *33* (20), 2007434. https://doi.org/10.1002/adma.202007434.

(20) Idrees, F.; Cao, C.; Butt, F. K.; Tahir, M.; Tanveer, M.; Aslam, I.; Ali, Z.; Mahmood, T.; Hou, J. Facile Synthesis of Novel Nb_3O_7F Nanoflowers, Their Optical and Photocatalytic Properties. *CrystEngComm* **2013**, *15* (40), 8146. https://doi.org/10.1039/c3ce41210e.

(21) Huang, F.; Zhao, H.; Yan, A.; Li, Z.; Liang, H.; Gao, Q.; Qiang, Y. In Situ Thermal Decomposition for Preparation of Nb_3O_7F/Nb_2O_5 Hybrid Nanomaterials with Enhanced Photocatalytic Performance. *Journal of Alloys and Compounds* **2017**, *695*, 489–495. https://doi.org/10.1016/j.jallcom.2016.11.113.

(22) Mizoguchi, H.; Orita, M.; Hirano, M.; Fujitsu, S.; Takeuchi, T.; Hosono, H. NbO_2F: An Oxyfluoride Phase with Wide Band Gap and Electrochromic Properties. *Appl. Phys. Lett.* **2002**, *80* (25), 4732–4734. https://doi.org/10.1063/1.1489703.

(23) Tao, J. Z.; Sleight, A. W. Very Low Thermal Expansion in TaO_2F. *Journal of Solid State Chemistry* **2003**, *173* (1), 45–48. https://doi.org/10.1016/S0022-4596(03)00077-X.

(24) Sawhill, S.; Savrun, E. A near Zero Coefficient of Thermal Expansion Ceramic: Tantalum Oxyfluoride. *Ceramics International* **2012**, *38* (3), 1981–1989. https://doi.org/10.1016/j.ceramint.2011.10.032.

(25) Morelock, C. R.; Greve, B. K.; Cetinkol, M.; Chapman, K. W.; Chupas, P. J.; Wilkinson, A. P. Role of Anion Site Disorder in the Near Zero Thermal Expansion of Tantalum Oxyfluoride. *Chem. Mater.* **2013**, *25* (9), 1900–1904. https://doi.org/10.1021/cm400536n.

(26) Bohnke, C.; Fourquet, J. L.; Randrianantoandro, N.; Brousse, T.; Crosnier, O. Electrochemical Intercalation of Lithium into the Perovskite-Type NbO_2F: Influence of the NbO_2F Particle Size. *J. Solid State Electrochem.* **2001**, *5* (1), 1–7. https://doi.org/10.1007/PL00010799.

(27) Bashian, N. H.; Preefer, M. B.; Milam-Guerrero, J.; Zak, J. J.; Sendi, C.; Ahsan, S. A.; Vincent, R. C.; Haiges, R.; See, K. A.; Seshadri, R.; Melot, B. C. Understanding the Role of

Crystallographic Shear on the Electrochemical Behavior of Niobium Oxyfluorides. *J. Mater. Chem. A* **2020**, *8* (25), 12623–12632. https://doi.org/10.1039/D0TA01406K.

(28) Permér, L. Li-Inserted Nb_3O_7F and Its Thermal Decomposition Products Studied by High-Resolution Electron Microscopy and X-Ray Powder Diffraction. *Journal of Solid State Chemistry* **1992**, *97* (1), 105–114. https://doi.org/10.1016/0022-4596(92)90014-M.

(29) Brink, F. J.; Withers, R. L.; Norén, L. An Electron Diffraction and Crystal Chemical Investigation of Oxygen/Fluorine Ordering in Niobium Oxyfluoride, NbO_2F. *Journal of Solid State Chemistry* **2002**, *166* (1), 73–80. https://doi.org/10.1006/jssc.2002.9562.

(30) Brink, F. J.; Withers, R. L.; Cordier, S.; Poulain, M. An Electron Diffraction and Bond Valence Sum Investigation of Oxygen/Fluorine Ordering in $NbnO_{2n-1}F_{n+2}$. *Journal of Solid State Chemistry* **2006**, *179* (2), 341–348. https://doi.org/10.1016/j.jssc.2005.10.014.

(31) Dabachi, J.; Body, M.; Galven, C.; Boucher, F.; Legein, C. Preparation-Dependent Composition and O/F Ordering in NbO_2F and TaO_2F. *Inorganic Chemistry* **2017**, *56* (9), 5219–5232. https://doi.org/10.1021/acs.inorgchem.7b00355.

(32) Brown, I. D.; Altermatt, D. Bond-Valence Parameters Obtained from a Systematic Analysis of the Inorganic Crystal Structure Database. *Acta Crystallographica Section B Structural Science* **1985**, *41* (4), 244–247. https://doi.org/10.1107/S0108768185002063.

(33) Brese, N. E.; O'Keeffe, M. Bond-Valence Parameters for Solids. *Acta Crystallographica Section B Structural Science* **1991**, *47* (2), 192–197. https://doi.org/10.1107/S0108768190011041.

(34) Goodwin, A. L. Opportunities and Challenges in Understanding Complex Functional Materials. *Nat Commun* **2019**, *10* (1), 4461. https://doi.org/10.1038/s41467-019-12422-z.

(35) Charpentier, T. The PAW/GIPAW Approach for Computing NMR Parameters: A New Dimension Added to NMR Study of Solids. *Solid State Nuclear Magnetic Resonance* **2011**, *40* (1), 1–20. https://doi.org/10.1016/j.ssnmr.2011.04.006.

(36) Bonhomme, C.; Gervais, C.; Babonneau, F.; Coelho, C.; Pourpoint, F.; Azaïs, T.; Ashbrook, S. E.; Griffin, J. M.; Yates, J. R.; Mauri, F.; Pickard, C. J. First-Principles Calculation of NMR Parameters Using the Gauge Including Projector Augmented Wave Method: A Chemist's Point of View. *Chem. Rev.* **2012**, *112* (11), 5733–5779. https://doi.org/10.1021/cr300108a.

(37) Ashbrook, S. E.; Dawson, D. M. Exploiting Periodic First-Principles Calculations in NMR Spectroscopy of Disordered Solids. *Acc. Chem. Res.* **2013**, *46* (9), 1964–1974. https://doi.org/10.1021/ar300303w.

(38) Moran, R. F.; Dawson, D. M.; Ashbrook, S. E. Exploiting NMR Spectroscopy for the Study of Disorder in Solids. *International Reviews in Physical Chemistry* **2017**, *36* (1), 39–115. https://doi.org/10.1080/0144235X.2017.1256604.

(39) Ashbrook, S. E.; Griffin, J. M.; Johnston, K. E. Recent Advances in Solid-State Nuclear Magnetic Resonance Spectroscopy. *Annual Rev. Anal. Chem.* **2018**, *11* (1), 485–508. https://doi.org/10.1146/annurev-anchem-061417-125852.

(40) Florian, P.; Veron, E.; Green, T. F. G.; Yates, J. R.; Massiot, D. Elucidation of the Al/Si Ordering in Gehlenite $Ca_2Al_2SiO_7$ by Combined ^{29}Si and ^{27}Al NMR Spectroscopy/Quantum Chemical Calculations. *Chem. Mater.* **2012**, *24* (21), 4068–4079. https://doi.org/10.1021/cm3016935.

(41) Ferrara, C.; Tealdi, C.; Pedone, A.; Menziani, M. C.; Rossini, A. J.; Pintacuda, G.; Mustarelli, P. Local versus Average Structure in $LaSrAl_3O_7$: A NMR and DFT Investigation. *J. Phys. Chem. C* **2013**, *117* (45), 23451–23458. https://doi.org/10.1021/jp403022j.

(42) Véron, E.; Garaga, M. N.; Pelloquin, D.; Cadars, S.; Suchomel, M.; Suard, E.; Massiot, D.; Montouillout, V.; Matzen, G.; Allix, M. Synthesis and Structure Determination of $CaSi_{1/3}B_{2/3}O_{8/3}$: A New Calcium Borosilicate. *Inorg. Chem.* **2013**, *52* (8), 4250–4258. https://doi.org/10.1021/ic302114t.

(43) Ashbrook, S. E.; Mitchell, M. R.; Sneddon, S.; Moran, R. F.; De Los Reyes, M.; Lumpkin, G. R.; Whittle, K. R. New Insights into Phase Distribution, Phase Composition and Disorder in $Y_2(Zr,Sn)_2O_7$ Ceramics from NMR Spectroscopy. *Phys. Chem. Chem. Phys.* **2015**, *17* (14), 9049–9059. https://doi.org/10.1039/C4CP05827E.

(44) Playford, Helen. Y.; Hannon, A. C.; Tucker, M. G.; Dawson, D. M.; Ashbrook, S. E.; Kastiban, R. J.; Sloan, J.; Walton, R. I. Characterization of Structural Disorder in γ-Ga_2O_3. *J. Phys. Chem. C* **2014**, *118* (29), 16188–16198. https://doi.org/10.1021/jp5033806.

(45) Flemming, R. L.; Terskikh, V.; Ye, E. Aluminum Environments in Synthetic Ca-Tschermak Clinopyroxene ($CaAlAlSiO_6$) from Rietveld Refinement, ^{27}Al NMR, and First-Principles Calculations. *American Mineralogist* **2015**, *100* (10), 2219–2230. https://doi.org/10.2138/am-2015-5348.

(46) Diez-Gómez, V.; Arbi, K.; Sanz, J. Modeling Ti/Ge Distribution in $LiTi_{2-x}Ge_x(PO_4)_3$ NASICON Series by ^{31}P MAS NMR and First-Principles DFT Calculations. *J. Am. Chem. Soc.* **2016**, *138* (30), 9479–9486. https://doi.org/10.1021/jacs.6b03583.

(47) Fernandes, A.; McKay, D.; Sneddon, S.; Dawson, D. M.; Lawson, S.; Veazey, R.; Whittle, K. R.; Ashbrook, S. E. Phase Composition and Disorder in $La_2(Sn,Ti)_2O_7$ Ceramics: New Insights from NMR Crystallography. *J. Phys. Chem. C* **2016**, *120* (36), 20288–20296. https://doi.org/10.1021/acs.jpcc.6b06962.

(48) Moran, R. F.; McKay, D.; Pickard, C. J.; Berry, A. J.; Griffin, J. M.; Ashbrook, S. E. Hunting for Hydrogen: Random Structure Searching and Prediction of NMR Parameters of Hydrous Wadsleyite. *Phys. Chem. Chem. Phys.* **2016**, *18* (15), 10173–10181. https://doi.org/10.1039/C6CP01529H.

(49) Fernandez-Carrion, A. J.; Al Saghir, K.; Veron, E.; Becerro, A. I.; Porcher, F.; Wisniewski, W.; Matzen, G.; Fayon, F.; Allix, M. Local Disorder and Tunable Luminescence in $Sr_{1-x/2}Al_{2-x}Si_xO_4$ ($0.2 \leq x \leq 0.5$) Transparent Ceramics. *Inorg. Chem.* **2017**, *56* (23), 14446–14458. https://doi.org/10.1021/acs.inorgchem.7b01881.

(50) Cadars, S.; Ahn, N. H.; Okhotnikov, K.; Shin, J.; Vicente, A.; Hong, S. B.; Fernandez, C. Modeling Short-Range Substitution Order and Disorder in Crystals: Application to the Ga/Si Distribution in a Natrolite Zeolite. *Solid State Nuclear Magnetic Resonance* **2017**, *84*, 182–195. https://doi.org/10.1016/j.ssnmr.2017.04.001.

(51) Girard, G.; Vasconcelos, F.; Montagne, L.; Delevoye, L. 31P MAS NMR Spectroscopy with 93Nb Decoupling and DFT Calculations: A Structural Characterization of Defects in a Niobium-Phosphate Phase. *Solid State Nuclear Magnetic Resonance* **2017**, *84*, 210–215. https://doi.org/10.1016/j.ssnmr.2017.05.003.

(52) Grüninger, H.; Armstrong, K.; Greim, D.; Boffa-Ballaran, T.; Frost, D. J.; Senker, J. Hidden Oceans? Unraveling the Structure of Hydrous Defects in the Earth's Deep Interior. *J. Am. Chem. Soc.* **2017**, *139* (30), 10499–10505. https://doi.org/10.1021/jacs.7b05432.

(53) Fischer, M. Local Environment and Dynamic Behavior of Fluoride Anions in Silicogermanate Zeolites: A Computational Study of the AST Framework. *J. Phys. Chem. C* **2019**, *123* (3), 1852–1865. https://doi.org/10.1021/acs.jpcc.8b10770.

(54) McKay, D.; Moran, R. F.; Dawson, D. M.; Griffin, J. M.; Sturniolo, S.; Pickard, C. J.; Berry, A. J.; Ashbrook, S. E. A Picture of Disorder in Hydrous Wadsleyite—Under the Combined Microscope of Solid-State NMR Spectroscopy and *Ab Initio* Random Structure Searching. *J. Am. Chem. Soc.* **2019**, *141* (7), 3024–3036. https://doi.org/10.1021/jacs.8b11519.

(55) Moran, R. F.; McKay, D.; Tornstrom, P. C.; Aziz, A.; Fernandes, A.; Grau-Crespo, R.; Ashbrook, S. E. Ensemble-Based Modeling of the NMR Spectra of Solid Solutions: Cation Disorder in $Y_2(Sn,Ti)_2O_7$. *J. Am. Chem. Soc.* **2019**, *141* (44), 17838–17846. https://doi.org/10.1021/jacs.9b09036.

(56) Serrano-Sevillano, J.; Carlier, D.; Saracibar, A.; Lopez Del Amo, J. M.; Casas-Cabanas, M. DFT-Assisted Solid-State NMR Characterization of Defects in Li_2MnO_3. *Inorg. Chem.* **2019**, *58* (13), 8347–8356. https://doi.org/10.1021/acs.inorgchem.9b00394.

(57) Moran, R. F.; Fernandes, A.; Dawson, D. M.; Sneddon, S.; Gandy, A. S.; Reeves-McLaren, N.; Whittle, K. R.; Ashbrook, S. E. Phase Distribution, Composition, and Disorder in $Y_2(Hf,Sn)_2O_7$ Ceramics: Insights from Solid-State NMR Spectroscopy and First-Principles Calculations. *J. Phys. Chem. C* **2020**, *124* (31), 17073–17084. https://doi.org/10.1021/acs.jpcc.0c04542.

(58) Ashbrook, S. E.; Dawson, D. M.; Gan, Z.; Hooper, J. E.; Hung, I.; Macfarlane, L. E.; McKay, D.; McLeod, L. K.; Walton, R. I. Application of NMR Crystallography to Highly Disordered Templated Materials: Extensive Local Structural Disorder in the Gallophosphate GaPO-34A. *Inorg. Chem.* **2020**, *59* (16), 11616–11626. https://doi.org/10.1021/acs.inorgchem.0c01450.

(59) Camus-Génot, V.; Guiet, A.; Lhoste, J.; Fayon, F.; Body, M.; Kodjikian, S.; Moury, R.; Leblanc, M.; Bobet, J. L.; Legein, C.; Maisonneuve, V. Controlled Morphology Synthesis of Nanostructured β-$AlF_{3-x}(OH)_x$ with Tunable Specific Surface Area. *Crystal Growth and Design* **2021**, *21* (10), 5914–5927. https://doi.org/10.1021/acs.cgd.1c00808.

(60) Fischer, M. Fluoride Anions in All-Silica Zeolites: Studying Preferred Fluoride Sites and Dynamic Disorder with Density Functional Theory Calculations. *J. Phys. Chem. C* **2021**, *125* (16), 8825–8839. https://doi.org/10.1021/acs.jpcc.1c01440.

(61) Hancock, J. C.; Griffith, K. J.; Choi, Y.; Bartel, C. J.; Lapidus, S. H.; Vaughey, J. T.; Ceder, G.; Poeppelmeier, K. R. Expanding the Ambient-Pressure Phase Space of $CaFe_2O_4$ -Type Sodium Postspinel Host–Guest Compounds. *ACS Org. Inorg. Au* **2022**, *2* (1), 8–22. https://doi.org/10.1021/acsorginorgau.1c00019.

(62) Leube, B. T.; Collins, C. M.; Daniels, L. M.; Duff, B. B.; Dang, Y.; Chen, R.; Gaultois, M. W.; Manning, T. D.; Blanc, F.; Dyer, M. S.; Claridge, J. B.; Rosseinsky, M. J. Cation Disorder and Large Tetragonal Supercell Ordering in the Li-Rich Argyrodite $Li_7Zn_{0.5}SiS_6$. *Chem. Mater.* **2022**, *34* (9), 4073–4087. https://doi.org/10.1021/acs.chemmater.2c00320.

(63) Pickard, C. J.; Mauri, F. All-Electron Magnetic Response with Pseudopotentials: NMR Chemical Shifts. *Physical Review B* **2001**, *63* (24). https://doi.org/10.1103/PhysRevB.63.245101.

(64) Yates, J. R.; Pickard, C. J.; Mauri, F. Calculation of NMR Chemical Shifts for Extended Systems Using Ultrasoft Pseudopotentials. *Physical Review B* **2007**, *76* (2). https://doi.org/10.1103/PhysRevB.76.024401.

(65) Galissard de Marignac, J.-C. Untersuchungen Über Die Verbindungen Des Niobiums. *Journal für praktische Chemie* **1866**, *97*, 449–465.

(66) Schäfer, H. Der Transport Anorganischer Stoffe Über Die Gasphase Und Seine Anwendungen. *Chemische Transportreaktionen* **1962**.

(67) Schäfer, H.; Schnering, H. G.; Niehues, K.-J.; Nieder-Vahrenholz, H. G. Beiträge zur chemie der elemente niob und tantal. *Journal of the Less Common Metals* **1965**, *9* (2), 95–104. https://doi.org/10.1016/0022-5088(65)90087-1.

(68) Nieder-Vahrenholz, H.-G.; Schäfer, H. Die Oxidfluoride des Niobs und Tantals. *Z. Anorg. Allg. Chem.* **1987**, *544* (1), 122–126. https://doi.org/10.1002/zaac.19875440113.

(69) Wilkinson, A. P.; Josefsberg, R. E.; Gallington, L. C.; Morelock, C. R.; Monaco, C. M. History-Dependent Thermal Expansion in NbO_2F. *Journal of Solid State Chemistry* **2014**, *213*, 38–42. https://doi.org/10.1016/j.jssc.2014.02.003.

(70) Herzfeld, J.; Berger, A. E. Sideband Intensities in NMR Spectra of Samples Spinning at the Magic Angle. *The Journal of Chemical Physics* **1980**, *73* (12), 6021–6030. https://doi.org/10.1063/1.440136.

(71) Massiot, D.; Hiet, J.; Pellerin, N.; Fayon, F.; Deschamps, M.; Steuernagel, S.; Grandinetti, P. J. Two-Dimensional One Pulse MAS of Half-Integer Quadrupolar Nuclei. *Journal of Magnetic Resonance* **2006**, *181* (2), 310–315. https://doi.org/10.1016/j.jmr.2006.05.007.

(72) Massiot, D.; Fayon, F.; Capron, M.; King, I.; Le Calvé, S.; Alonso, B.; Durand, J.-O.; Bujoli, B.; Gan, Z.; Hoatson, G. Modelling One- and Two-Dimensional Solid-State NMR Spectra. *Magnetic Resonance in Chemistry* **2002**, *40* (1), 70–76. https://doi.org/10.1002/mrc.984.

(73) Haeberlen, U. Advances in Magnetic Resonance; Suppl. 1; Academic Press: New York, 1976.

(74) Perdew, J. P.; Burke, K.; Ernzerhof, M. Generalized Gradient Approximation Made Simple. *Physical Review Letters* **1996**, *77* (18), 3865–3868. https://doi.org/10.1103/PhysRevLett.77.3865.

(75) Kresse, G.; Furthmüller, J. Efficiency of Ab-Initio Total Energy Calculations for Metals and Semiconductors Using a Plane-Wave Basis Set. *Computational Materials Science* **1996**, *6* (1), 15–50. https://doi.org/10.1016/0927-0256(96)00008-0.

(76) Kresse, G.; Furthmüller, J. Efficient Iterative Schemes for *Ab Initio* Total-Energy Calculations Using a Plane-Wave Basis Set. *Phys. Rev. B* **1996**, *54* (16), 11169–11186. https://doi.org/10.1103/PhysRevB.54.11169.

(77) Blöchl, P. E. Projector Augmented-Wave Method. *Phys. Rev. B* **1994**, *50* (24), 17953–17979. https://doi.org/10.1103/PhysRevB.50.17953.

(78) Kresse, G.; Joubert, D. From Ultrasoft Pseudopotentials to the Projector Augmented-Wave Method. *Phys. Rev. B* **1999**, *59* (3), 1758–1775. https://doi.org/10.1103/PhysRevB.59.1758.

(79) Grimme, S.; Antony, J.; Ehrlich, S.; Krieg, H. A Consistent and Accurate *Ab Initio* Parametrization of Density Functional Dispersion Correction (DFT-D) for the 94 Elements H-Pu. *The Journal of Chemical Physics* **2010**, *132* (15), 154104. https://doi.org/10.1063/1.3382344.

(80) Griffin, J. M.; Yates, J. R.; Berry, A. J.; Wimperis, S.; Ashbrook, S. E. High-Resolution ^{19}F MAS NMR Spectroscopy: Structural Disorder and Unusual *J* Couplings in a Fluorinated Hydroxy-Silicate. *J. Am. Chem. Soc.* **2010**, *132* (44), 15651–15660. https://doi.org/10.1021/ja105347q.

(81) Sadoc, A.; Body, M.; Legein, C.; Biswal, M.; Fayon, F.; Rocquefelte, X.; Boucher, F. NMR Parameters in Alkali, Alkaline Earth and Rare Earth Fluorides from First Principle Calculations. *Physical Chemistry Chemical Physics* **2011**, *13* (41), 18539. https://doi.org/10.1039/c1cp21253b.

(82) Pedone, A.; Charpentier, T.; Menziani, M. C. The Structure of Fluoride-Containing Bioactive Glasses: New Insights from First-Principles Calculations and Solid State NMR Spectroscopy. *J. Mater. Chem.* **2012**, *22* (25), 12599. https://doi.org/10.1039/c2jm30890h.

(83) Biswal, M.; Body, M.; Legein, C.; Sadoc, A.; Boucher, F. NbF_5 and TaF_5: Assignment of ^{19}F NMR Resonances and Chemical Bond Analysis from GIPAW Calculations. *Journal of Solid State Chemistry* **2013**, *207*, 208–217. https://doi.org/10.1016/j.jssc.2013.09.001.

(84) Sadoc, A.; Biswal, M.; Body, M.; Legein, C.; Boucher, F.; Massiot, D.; Fayon, F. NMR Parameters in Column 13 Metal Fluoride Compounds (AlF_3, GaF_3, InF_3 and TlF) from First Principle Calculations. *Solid State Nuclear Magnetic Resonance* **2014**, *59–60*, 1–7. https://doi.org/10.1016/j.ssnmr.2014.01.001.

(85) Rakhmatullin, A.; Boča, M.; Mlynáriková, J.; Hadzimová, E.; Vasková, Z.; Polovov, I. B.; Mičušík, M. Solid State NMR and XPS of Ternary Fluorido-Zirconates of Various Coordination Modes. *Journal of Fluorine Chemistry* **2018**, *208*, 24–35. https://doi.org/10.1016/j.jfluchem.2018.01.010.

(86) Rakhmatullin, A.; Polovov, I. B.; Maltsev, D.; Allix, M.; Volkovich, V.; Chukin, A. V.; Boča, M.; Bessada, C. Combined Approach for the Structural Characterization of Alkali Fluoroscandates: Solid-State NMR, Powder X-Ray Diffraction, and Density Functional Theory Calculations. *Inorg. Chem.* **2018**, *57* (3), 1184–1195. https://doi.org/10.1021/acs.inorgchem.7b02617.

(87) Martel, L.; Capelli, E.; Body, M.; Klipfel, M.; Beneš, O.; Maksoud, L.; Raison, P. E.; Suard, E.; Visscher, L.; Bessada, C.; Legein, C.; Charpentier, T.; Kovács, A. Insight into the Crystalline Structure of ThF_4 with the Combined Use of Neutron Diffraction, ^{19}F Magic-Angle Spinning-NMR, and Density Functional Theory Calculations. *Inorganic Chemistry* **2018**, *57* (24), 15350–15360. https://doi.org/10.1021/acs.inorgchem.8b02683.

(88) DeVore, M. A.; Klug, C. A.; Kriz, M. R.; Roy, L. E.; Wellons, M. S. Investigations of Uranyl Fluoride Sesquihydrate ($UO_2F_2{\cdot}1.57H_2O$): Combining ^{19}F Solid-State MAS NMR Spectroscopy and GIPAW Chemical Shift Calculations. *J. Phys. Chem. A* **2018**, *122* (34), 6873–6878. https://doi.org/10.1021/acs.jpca.8b04369.

(89) Dabachi, J.; Body, M.; Dittmer, J.; Rakhmatullin, A.; Fayon, F.; Legein, C. Insight into the Factors Influencing NMR Parameters in Crystalline Materials from the $KF{-}YF_3$ Binary System. *Dalton Transactions* **2019**, *48* (2), 587–601. https://doi.org/10.1039/C8DT03241F.

(90) Murakami, M.; Noda, Y.; Takegoshi, K. Terminal and Bridging Fluorine Ligands in TiF_4 as Studied by ^{19}F NMR in Solids. *Solid State Nuclear Magnetic Resonance* **2019**, *101*, 82–88. https://doi.org/10.1016/j.ssnmr.2019.05.007.

(91) Ding, F.; Griffith, K. J.; Koçer, C. P.; Saballos, R. J.; Wang, Y.; Zhang, C.; Nisbet, M. L.; Morris, A. J.; Rondinelli, J. M.; Poeppelmeier, K. R. Multimodal Structure Solution with ^{19}F NMR

Crystallography of Spin Singlet Molybdenum Oxyfluorides. *J. Am. Chem. Soc.* **2020**, *142* (28), 12288–12298. https://doi.org/10.1021/jacs.0c04019.

(92) Legein, C.; Body, M.; Lhoste, J.; Li, W.; Charpentier, T.; Dambournet, D. Synthesis, Crystal Structure and ^{19}F NMR Parameters Modelling of $CaTiF_6(H_2O)_2$ Yielding to a Revision of the Bond-Valence Parameters for the Ti^{4+}/F<sub>–</sup> ion pair. *Journal of Solid State Chemistry* **2023**, *319*, 123793. https://doi.org/10.1016/j.jssc.2022.123793.

(93) Segall, M. D.; Lindan, P. J. D.; Probert, M. J.; Pickard, C. J.; Hasnip, P. J.; Clark, S. J.; Payne, M. C. First-Principles Simulation: Ideas, Illustrations and the CASTEP Code. *J. Phys.: Condens. Matter* **2002**, *14* (11), 2717–2744. https://doi.org/10.1088/0953-8984/14/11/301.

(94) Clark, S. J.; Segall, M. D.; Pickard, C. J.; Hasnip, P. J.; Probert, M. I. J.; Refson, K.; Payne, M. C. First Principles Methods Using CASTEP. *Zeitschrift für Kristallographie - Crystalline Materials* **2005**, *220* (5/6). https://doi.org/10.1524/zkri.220.5.567.65075.

(95) Gervais, C.; Profeta, M.; Lafond, V.; Bonhomme, C.; Azaïs, T.; Mutin, H.; Pickard, C. J.; Mauri, F.; Babonneau, F. Combined Ab Initio Computational and Experimental Multinuclear Solid-State Magnetic Resonance Study of Phenylphosphonic Acid. *Magnetic Resonance in Chemistry* **2004**, *42* (5), 445–452. https://doi.org/10.1002/mrc.1360.

(96) Li, W.; Corradini, D.; Body, M.; Legein, C.; Salanne, M.; Ma, J.; Chapman, K. W.; Chupas, P. J.; Rollet, A.-L.; Julien, C.; Zhagib, K.; Duttine, M.; Demourgues, A.; Groult, H.; Dambournet, D. High Substitution Rate in TiO_2 Anatase Nanoparticles with Cationic Vacancies for Fast Lithium Storage. *Chem. Mater.* **2015**, *27* (14), 5014–5019. https://doi.org/10.1021/acs.chemmater.5b01407.

(97) Berglund, B.; Vaughan, R. W. Correlations between Proton Chemical Shift Tensors, Deuterium Quadrupole Couplings, and Bond Distances for Hydrogen Bonds in Solids. *The Journal of Chemical Physics* **1980**, *73* (5), 2037–2043. https://doi.org/10.1063/1.440423.

(98) Eckert, H.; Yesinowski, J. P.; Silver, L. A.; Stolper, E. M. Water in Silicate Glasses: Quantitation and Structural Studies by Proton Solid Echo and Magic Angle Spinning NMR Methods. *J. Phys. Chem.* **1988**, *92* (7), 2055–2064. https://doi.org/10.1021/j100318a070.

(99) Harris, R. K.; Jackson, P.; Merwin, L. H.; Say, B. J.; Hägele, G. Perspectives in High-Resolution Solid-State Nuclear Magnetic Resonance, with Emphasis on Combined Rotation and Multiple-Pulse Spectroscopy. *J. Chem. Soc., Faraday Trans. 1* **1988**, *84* (11), 3649. https://doi.org/10.1039/f19888403649.

(100)Dalvit, C.; Vulpetti, A. Fluorine-Protein Interactions and ^{19}F NMR Isotropic Chemical Shifts: An Empirical Correlation with Implications for Drug Design. *ChemMedChem* **2011**, *6* (1), 104–114. https://doi.org/10.1002/cmdc.201000412.

(101)Rietveld, H. M. A Profile Refinement Method for Nuclear and Magnetic Structures. *J Appl Crystallogr* **1969**, *2* (2), 65–71. https://doi.org/10.1107/S0021889869006558.

(102)Rodriguez-Carvajal, J. Magnetic Structure Determination from Powder Diffraction Using the Program *FullProf*. In *Applied Crystallography*; WORLD SCIENTIFIC: Wisla, Poland, 2001; pp 30–36. https://doi.org/10.1142/9789812811325_0005.

(103)Groom, C. R.; Bruno, I. J.; Lightfoot, M. P.; Ward, S. C. The Cambridge Structural Database. *Acta Crystallogr B Struct Sci Cryst Eng Mater* **2016**, *72* (2), 171–179. https://doi.org/10.1107/S2052520616003954.

(104)Okhotnikov, K.; Charpentier, T.; Cadars, S. Supercell Program: A Combinatorial Structure-Generation Approach for the Local-Level Modeling of Atomic Substitutions and Partial Occupancies in Crystals. *J Cheminform* **2016**, *8* (1), 17. https://doi.org/10.1186/s13321-016-0129-3.

Table of Contents Synopsis.

MOF$_3$ (M = Nb, Ta) compounds were precisely modeled by combining powder X-Ray diffraction, solid-state NMR spectroscopy and semi-empirical dispersion corrected DFT calculations. *cis*-MO$_2$F$_4$ octahedra are favored, resulting in O/F correlated disorder. Some of the bridging F atoms are substituted by OH groups, especially in NbOF$_3$. Hydroxylated NbOF$_3$ was then successfully modeled highlighting that each H atom is either strongly H bonded to one F2 atom or in contact with four F2 atoms.

Table of Contents Graphic.